

Gaia Early Data Release 3

The Galactic anticentre★

Gaia Collaboration: T. Antoja^{1,★★}, P. J. McMillan², G. Kordopatis³, P. Ramos¹, A. Helmi⁴, E. Balbinot⁴, T. Cantat-Gaudin¹, L. Chemin⁵, F. Figueras¹, C. Jordi¹, S. Khanna⁴, M. Romero-Gómez¹, G. M. Seabroke⁶, A. G. A. Brown⁷, A. Vallenari⁸, T. Prusti⁹, J. H. J. de Bruijne⁹, C. Babusiaux^{10,11}, M. Biermann¹², O. L. Creevey³, D. W. Evans¹³, L. Eyer¹⁴, A. Hutton¹⁵, F. Jansen⁹, S. A. Klioner¹⁶, U. Lammers¹⁷, L. Lindegren², X. Luri¹, F. Mignard³, C. Panem¹⁸, D. Pourbaix^{19,20}, S. Randich²¹, P. Sartoretti¹¹, C. Soubiran²², N. A. Walton¹³, F. Arenou¹¹, C. A. L. Bailer-Jones²³, U. Bastian¹², M. Cropper⁶, R. Drimmel²⁴, D. Katz¹¹, M. G. Lattanzi^{24,25}, F. van Leeuwen¹³, J. Bakker¹⁷, J. Castañeda²⁶, F. De Angeli¹³, C. Ducourant²², C. Fabricius¹, M. Fouesneau²³, Y. Frémat²⁷, R. Guerra¹⁷, A. Guerrier¹⁸, J. Guiraud¹⁸, A. Jean-Antoine Piccolo¹⁸, E. Masana¹, R. Messineo²⁸, N. Mowlavi¹⁴, C. Nicolas¹⁸, K. Nienartowicz^{29,30}, F. Pailler¹⁸, P. Panuzzo¹¹, F. Riclet¹⁸, W. Roux¹⁸, R. Sordo⁸, P. Tanga³, F. Thévenin³, G. Gracia-Abriú^{31,12}, J. Portell¹, D. Teyssier³², M. Altmann^{12,33}, R. Andrae²³, I. Bellas-Velidis³⁴, K. Benson⁶, J. Berthier³⁵, R. Blomme²⁷, E. Brugaletta³⁶, P. W. Burgess¹³, G. Busso¹³, B. Carry³, A. Cellino²⁴, N. Cheek³⁷, G. Clementini³⁸, Y. Damerdjji^{39,40}, M. Davidson⁴¹, L. Delchambre³⁹, A. Dell’Oro²¹, J. Fernández-Hernández⁴², L. Galluccio³, P. García-Lario¹⁷, M. García-Reinaldos¹⁷, J. González-Núñez^{37,43}, E. Gosset^{39,20}, R. Haigron¹¹, J.-L. Halbwachs⁴⁴, N. C. Hambly⁴¹, D. L. Harrison^{13,45}, D. Hatzidimitriou⁴⁶, U. Heiter⁴⁷, J. Hernández¹⁷, D. Hestroffer³⁵, S. T. Hodgkin¹³, B. Holl^{14,29}, K. Janßen⁴⁸, G. Jevardat de Fombelle¹⁴, S. Jordan¹², A. Krone-Martins^{49,50}, A. C. Lanzafame^{36,51}, W. Löffler¹², A. Lorca¹⁵, M. Manteiga⁵², O. Marchal⁴⁴, P. M. Marrese^{53,54}, A. Moitinho⁴⁹, A. Mora¹⁵, K. Muinonen^{55,56}, P. Osborne¹³, E. Pancino^{21,54}, T. Pauwels²⁷, A. Recio-Blanco³, P. J. Richards⁵⁷, M. Riello¹³, L. Rimoldini²⁹, A. C. Robin⁵⁸, T. Roegiers⁵⁹, J. Rybizki²³, L. M. Sarro⁶⁰, C. Siopis¹⁹, M. Smith⁶, A. Sozzetti²⁴, A. Ulla⁶¹, E. Utrilla¹⁵, M. van Leeuwen¹³, W. van Reeve¹⁵, U. Abbas²⁴, A. Abreu Aramburu⁴², S. Accart⁶², C. Aerts^{63,64,23}, J. J. Aguado⁶⁰, M. Ajaj¹¹, G. Altavilla^{53,54}, M. A. Álvarez⁶⁵, J. Álvarez Cid-Fuentes⁶⁶, J. Alves⁶⁷, R. I. Anderson⁶⁸, E. Anglada Varela⁴², M. Audard²⁹, D. Baines³², S. G. Baker⁶, L. Balaguer-Núñez¹, Z. Balog^{12,23}, C. Barache³³, D. Barbato^{14,24}, M. Barros⁴⁹, M. A. Barstow⁶⁹, S. Bartolomé¹, J.-L. Bassilana⁶², N. Bauchet³⁵, A. Baudesson-Stella⁶², U. Becciani³⁶, M. Bellazzini³⁸, M. Bernet¹, S. Bertone^{70,71,24}, L. Bianchi⁷², S. Blanco-Cuaresma⁷³, T. Boch⁴⁴, A. Bombrun⁷⁴, D. Bossini⁷⁵, S. Bouquillon³³, A. Bragaglia³⁸, L. Bramante²⁸, E. Breedt¹³, A. Bressan⁷⁶, N. Brouillet²², B. Bucciarelli²⁴, A. Burlacu⁷⁷, D. Busonero²⁴, A. G. Butkevich²⁴, R. Buzzzi²⁴, E. Caffau¹¹, R. Cancelliere⁷⁸, H. Cánovas¹⁵, R. Carballo⁷⁹, T. Carlucci³³, M. I. Carnerero²⁴, J. M. Carrasco¹, L. Casamiquela²², M. Castellani⁵³, A. Castro-Ginard¹, P. Castro Sampedo¹, L. Chaoul¹⁸, P. Charlot²², A. Chiavassa³, M.-R. L. Cioni⁴⁸, G. Comoretto⁸⁰, W. J. Cooper^{81,24}, T. Cornez⁶², S. Cowell¹³, F. Crifo¹¹, M. Crosta²⁴, C. Crowley⁷⁴, C. Dafonte⁶⁵, A. Dapergolas³⁴, M. David⁸², P. David³⁵, P. de Laverny³, F. De Luise⁸³, R. De March²⁸, J. De Ridder⁶³, R. de Souza⁸⁴, P. de Teodoro¹⁷, A. de Torres⁷⁴, E. F. del Peloso¹², E. del Pozo¹⁵, A. Delgado¹³, H. E. Delgado⁶⁰, J.-B. Delisle¹⁴, P. Di Matteo¹¹, S. Diakite⁸⁵, C. Diener¹³, E. Distefano³⁶, C. Dolding⁶, D. Eappachen^{86,64}, H. Enke⁴⁸, P. Esquej⁸⁷, C. Fabre⁸⁸, M. Fabrizio^{53,54}, S. Faigler⁸⁹, G. Fedorets^{55,90}, P. Fernique^{44,91}, A. Fienga^{92,35}, C. Fouron⁷⁷, F. Fragkoudi⁹³, E. Fraile⁸⁷, F. Franke⁹⁴, M. Gai²⁴, D. Garabato⁶⁵, A. Garcia-Gutierrez¹, M. García-Torres⁹⁵, A. Garofalo³⁸, P. Gavras⁸⁷, E. Gerlach¹⁶, R. Geyer¹⁶, P. Giacobbe²⁴, G. Gilmore¹³, S. Girona⁶⁶, G. Giuffrida⁵³, A. Gomez⁶⁵, I. Gonzalez-Santamaria⁶⁵, J. J. González-Vidal¹, M. Granvik^{55,96}, R. Gutiérrez-Sánchez³², L. P. Guy^{29,80}, M. Hauser^{23,97}, M. Haywood¹¹, S. L. Hidalgo^{98,99}, T. Hilger¹⁶, N. Hładczuk¹⁷, D. Hobbs², G. Holland¹³, H. E. Huckle⁶, G. Jasniewicz¹⁰⁰, P. G. Jonker^{64,86}, J. Juaristi Campillo¹², F. Julbe¹, L. Karbevská¹⁴, P. Kervella¹⁰¹, A. Kochoska¹⁰², M. Kontizas⁴⁶, A. J. Korn⁴⁷, Z. Kostrzewa-Rutkowska^{7,86}, K. Kruszyńska¹⁰³, S. Lambert³³, A. F. Lanza³⁶, Y. Lasne⁶², J.-F. Le Campion¹⁰⁴, Y. Le Fustec⁷⁷, Y. Lebreton^{101,105}, T. Lebzelter⁶⁷, S. Leccia¹⁰⁶, N. Leclerc¹¹, I. Lecoœur-Taïbi²⁹, S. Liao²⁴, E. Licata²⁴, H. E. P. Lindstrøm^{24,107}, T. A. Lister¹⁰⁸, E. Livanou⁴⁶, A. Lobel²⁷, P. Madrero Pardo¹, S. Managau⁶², R. G. Mann⁴¹, J. M. Marchant¹⁰⁹, M. Marconi¹⁰⁶, M. M. S. Marcos Santos³⁷, S. Marinoni^{53,54}, F. Marocco^{110,111}, D. J. Marshall¹¹², L. Martin Polo³⁷, J. M. Martín-Fleitas¹⁵, A. Masip¹, D. Massari³⁸, A. Mastrobuono-Battisti², T. Mazeh⁸⁹, S. Messina³⁶, D. Michalik⁹, N. R. Millar¹³, A. Mints⁴⁸, D. Molina¹

* Movie is available at <https://www.aanda.org>

** Corresponding author: T. Antoja, e-mail: tantoja@fqa.ub.edu

R. Molinaro¹⁰⁶, L. Molnár^{113,114,115}, P. Montegriffo³⁸, R. Mor¹, R. Morbidelli²⁴, T. Morel³⁹, D. Morris⁴¹, A. F. Mulone²⁸, D. Muñoz⁶², T. Muraveva³⁸, C. P. Murphy¹⁷, I. Musella¹⁰⁶, L. Noval⁶², C. Ordénovic³, G. Orrù²⁸, J. Osinde⁸⁷, C. Pagani⁶⁹, I. Pagano³⁶, L. Palaversa^{116,13}, P. A. Palicio³, A. Panahi⁸⁹, M. Pawlak^{117,103}, X. Peñalosa Esteller¹, A. Penttilä⁵⁵, A. M. Piersimoni⁸³, F.-X. Pineau⁴⁴, E. Plachy^{113,114,115}, G. Plum¹¹, E. Poggio²⁴, E. Poretti¹¹⁸, E. Poujoulet¹¹⁹, A. Prša¹⁰², L. Pulone⁵³, E. Racero^{37,120}, S. Ragaini³⁸, M. Rainer²¹, C. M. Raiteri²⁴, N. Rambaux³⁵, M. Ramos-Lerate¹²¹, P. Re Fiorentin²⁴, S. Regibo⁶³, C. Reylé⁵⁸, V. Ripepi¹⁰⁶, A. Riva²⁴, G. Rixon¹³, N. Robichon¹¹, C. Robin⁶², M. Roelens¹⁴, L. Rohrbasser²⁹, N. Rowell⁴¹, F. Royer¹¹, K. A. Rybicki¹⁰³, G. Sadowski¹⁹, A. Sagristà Sellés¹², J. Sahlmann⁸⁷, J. Salgado³², E. Salguero⁴², N. Samaras²⁷, V. Sanchez Gimenez¹, N. Sanna²¹, R. Santoveña⁶⁵, M. Sarasso²⁴, M. Schultheis³, E. Sciacca³⁶, M. Segol⁹⁴, J. C. Segovia³⁷, D. Ségransan¹⁴, D. Semeux⁸⁸, H. I. Siddiqui¹²², A. Siebert^{44,91}, L. Siltala⁵⁵, E. Slezak³, R. L. Smart²⁴, E. Solano¹²³, F. Solitro²⁸, D. Souami^{101,124}, J. Souchay³³, A. Spagna²⁴, F. Spoto⁷³, I. A. Steele¹⁰⁹, H. Steidelmüller¹⁶, C. A. Stephenson³², M. Süveges^{29,125,23}, L. Szabados¹¹³, E. Szegedi-Elek¹¹³, F. Taris³³, G. Tauran⁶², M. B. Taylor¹²⁶, R. Teixeira⁸⁴, W. Thuillot³⁵, N. Tonello⁶⁶, F. Torra²⁶, J. Torra^{†,1}, C. Turon¹¹, N. Unger¹⁴, M. Vaillant⁶², E. van Dillen⁹⁴, O. Vanel¹¹, A. Vecchiato²⁴, Y. Viala¹¹, D. Vicente⁶⁶, S. Voutsinas⁴¹, M. Weiler¹, T. Wevers¹³, Ł. Wyrzykowski¹⁰³, A. Yoldas¹³, P. Yvard⁹⁴, H. Zhao³, J. Zorec¹²⁷, S. Zucker¹²⁸, C. Zurbach¹²⁹, and T. Zwitter¹³⁰

(Affiliations can be found after the references)

Received 19 October 2020 / Accepted 12 January 2021

ABSTRACT

Aims. We aim to demonstrate the scientific potential of the *Gaia* Early Data Release 3 (EDR3) for the study of different aspects of the Milky Way structure and evolution and we provide, at the same time, a description of several practical aspects of the data and examples of their usage.

Methods. We used astrometric positions, proper motions, parallaxes, and photometry from EDR3 to select different populations and components and to calculate the distances and velocities in the direction of the anticentre. In this direction, the *Gaia* astrometric data alone enable the calculation of the vertical and azimuthal velocities; also, the extinction is relatively low compared to other directions in the Galactic plane. We then explore the disturbances of the current disc, the spatial and kinematical distributions of early accreted versus in situ stars, the structures in the outer parts of the disc, and the orbits of open clusters Berkeley 29 and Saurer 1.

Results. With the improved astrometry and photometry of EDR3, we find that: (i) the dynamics of the Galactic disc are very complex with oscillations in the median rotation and vertical velocities as a function of radius, vertical asymmetries, and new correlations, including a bimodality with disc stars with large angular momentum moving vertically upwards from below the plane, and disc stars with slightly lower angular momentum moving preferentially downwards; (ii) we resolve the kinematic substructure (diagonal ridges) in the outer parts of the disc for the first time; (iii) the red sequence that has been associated with the proto-Galactic disc that was present at the time of the merger with *Gaia*-Enceladus-Sausage is currently radially concentrated up to around 14 kpc, while the blue sequence that has been associated with debris of the satellite extends beyond that; (iv) there are density structures in the outer disc, both above and below the plane, most probably related to Monoceros, the Anticentre Stream, and TriAnd, for which the *Gaia* data allow an exhaustive selection of candidate member stars and dynamical study; and (v) the open clusters Berkeley 29 and Saurer 1, despite being located at large distances from the Galactic centre, are on nearly circular disc-like orbits.

Conclusions. Even with our simple preliminary exploration of the *Gaia* EDR3, we demonstrate how, once again, these data from the European Space Agency are crucial for our understanding of the different pieces of our Galaxy and their connection to its global structure and history.

Key words. Galaxy: disk – Galaxy: halo – stars: distances – open clusters and associations: individual: Saurer 1 – open clusters and associations: individual: Berkeley 29 – Galaxy: kinematics and dynamics

1. Introduction

As for previous releases, the Early Third Data Release (EDR3, [Gaia Collaboration 2021a](#)) of the *Gaia* mission ([Gaia Collaboration 2016](#)) of the European Space Agency is accompanied with performance verification articles showing the quality of the data, the improvements with respect to previous releases, and the scientific potential for multiple research areas in astrophysics (see also [Gaia Collaboration 2021c,d,b](#)). In the present study we focus on a specific area in the sky that allows us to explore different elements of the Milky Way's (MW) structure and history: the Galactic anticentre. This region of the Galaxy has the advantage that from astrometric measurements alone (proper motions and parallaxes), one can calculate the vertical and azimuthal (rotation) motion of the stars with a negligible contribution of the line-of-sight velocity. Also, the anticentre

has relatively low extinction compared to other directions of the Galactic disc.

More importantly, the anticentre is a meeting point of several distinct components of the Galaxy (the disc, the halo) and possibly hosts ancient and recently disrupted stellar systems of extragalactic origin. The anticentre is also an excellent window to the dynamics and the past of the MW since, due to the lower gravitational potential, any perturbation on the disc would cause more significant deformations than in the inner disc, and, due to the longer dynamical timescales, these could still be observable today (e.g. [Binney & Tremaine 2008](#); [Antoja et al. 2018](#); [Laporte et al. 2019a](#)).

In this paper we focus on several aspects of the Galaxy that coexist in the anticentre and that will help us towards answering a single question: how the Galaxy appears today and how it became like this. Thanks to a combination of models and

[†]Deceased.

measurements, in which *Gaia* DR2 (Gaia Collaboration 2018b) played one of the most relevant roles, we have already uncovered part of the MW structure and history. The major accretion event of the so-called *Gaia*-Enceladus-Sausage around 10 Gyr ago (Helmi et al. 2018; Belokurov et al. 2018), together with the ongoing accretion of the Sagittarius dwarf galaxy (Mateo et al. 1996; Majewski et al. 2003 and a recent detection with *Gaia* data in Antoja et al. 2020), and internal structures such as the bar (de Vaucouleurs 1964; Binney et al. 1991; Blitz & Spergel 1991; Weiland et al. 1994) and the spiral arms (Drimmel & Spergel 2001; Reid et al. 2009) are among the most important phenomena that have shaped our Galaxy throughout its evolution (see also Bland-Hawthorn & Gerhard 2016). The footprints of these phenomena can still be observed today and that is what we investigate here.

First, we look into the kinematic disturbances of the disc that EDR3 allows us to inspect in its outermost parts with more detail. Already known disturbances include vertical asymmetries in the number counts linked to vertical bending and breathing waves (e.g. Widrow et al. 2012; Bennett & Bovy 2019), substructure in the in-plane velocities (e.g. Dehnen 1998; Famaey et al. 2005; Antoja et al. 2008, 2018; Kawata et al. 2018; Khanna et al. 2019a; Fragkoudi et al. 2019) large scale velocity patterns in the disc (Siebert et al. 2011; Williams et al. 2013; Carlin et al. 2013; Antoja et al. 2017) and other phase space correlations (e.g. Schönrich & Dehnen 2018; Friske & Schönrich 2019; Huang et al. 2018; Cheng et al. 2020). While some of these could be related to the structures such as the bar, the poorly-known spiral arms and the warp, more recently, the *Gaia* vertical phase spiral (Antoja et al. 2018; Bland-Hawthorn et al. 2019) suggests a phase mixing event after the perturbation of Sagittarius (Binney & Schönrich 2018; Laporte et al. 2019a). All of these have proven to be difficult to understand, and also to disentangle or relate. Here we look at the rotation and vertical velocities of the outer disc, showing the power that *Gaia* data can have in our understanding of this complexity and the role that recent and past, internal and external, perturbations have had in the MW.

Second, we go from the current disc of the Galaxy to more ancient components. Two distinct populations were clearly apparent in the Hertzsprung-Russell (HR) diagram of stars with large tangential velocities near the Sun (i.e. representing the stellar halo) by Gaia Collaboration (2018a) using *Gaia* DR2: a blue and a red sequence. It has been proposed that these two populations correspond to an accreted one stemming largely from the galaxy *Gaia*-Enceladus-Sausage, and an in situ heated (thick) disc, different from the canonical thick disc, that was present at the time of this merger (Helmi et al. 2018; Belokurov et al. 2018, 2020; Di Matteo et al. 2019; Gallart et al. 2019). Here we analyse the spatial distribution and kinematics of stars from each of the HR sequences to investigate out to which distance the debris of *Gaia*-Enceladus-Sausage may be found, and constrain the extent of the suggested proto-Galactic disc present at that time.

Thirdly, we explore the density structures that appear in the edge of the disc in the anticentre direction. Newberg et al. (2002) using the deep Sloan Digital Sky Survey (SDSS York et al. 2000) discovered the existence of a $\sim 100^\circ$ structure in their A and F star count maps. Now known as Monoceros, later studies have confirmed its existence and large extension on the sky (e.g. Crane et al. 2003; Yanny et al. 2003; Ibata et al. 2003). Together with the Anticentre stream (ACS, Grillmair 2006), both at a distance ~ 10 kpc from the Sun, and the Triangulum-Andromeda overdensities (TriAnd, Majewski et al. 2004; Rocha-Pinto et al. 2004; Martin et al. 2007), they are part of a complex and substructured outer disc. The initial interpretation that these could be the

remains of an accreted dwarf galaxy (e.g. Martin et al. 2004; Peñarrubia et al. 2005) has become less plausible (although not completely ruled out) since: (i) there is no known progenitor to the stream (the candidate Canis Major has been discarded – Momany et al. 2004, 2006; Rocha-Pinto et al. 2006), and (ii) the kinematics of the structures (e.g. de Boer et al. 2018), their metallicities and their ratio of RR Lyrae to Giants (Li et al. 2012; Sheffield et al. 2014, 2018; Price-Whelan et al. 2015; Bergemann et al. 2018; Laporte et al. 2020a) are compatible with that of the disc. Here we explore how these structures look in *Gaia* EDR3 and coexist with other structures such as the Sagittarius stream.

Finally, we explore the open clusters Berkeley 29 (Kaluzny 1994; Lata et al. 2002; Tosi et al. 2004; Bragaglia & Tosi 2006) and Saurer 1 (Frinchaboy & Phelps 2002; Carraro & Baume 2003) in the anticentre direction that, with ages of several Gyr, are among the oldest Galactic clusters known. Their unusual location at Galactocentric distances of ~ 20 kpc and more than 1 kpc above the Galactic mid-plane is a puzzle that has led several authors to question whether they are associated with the disc, and to propose a possible extragalactic origin (e.g. Frinchaboy et al. 2004). Attempts to characterise the orbits of these two objects have returned widely discrepant results (Carraro et al. 2007; Vande Putte et al. 2010), mainly due to their poorly-constrained proper motions since at such large distances, small proper motion errors translate into large uncertainties in physical velocities. An additional issue has been the uncertain membership status of individual stars. Here, thanks to *Gaia* EDR3, we perform a robust analysis of the membership of these clusters and derive their orbits with high confidence.

To investigate all these aspects, the main *Gaia* data products that we use here are the astrometric measurements. For EDR3 these show a substantial decrease of uncertainties resulting from the use of 34 months of data (12 more than for DR2). Apart from a higher completeness at the faint end, there is a significantly larger number of stars at a given parallax precision. The combination of all these improvements essentially means that we can now explore distant regions of the Galaxy in the direction of the anticentre, even reaching around 16 kpc from the Galactic centre and beyond (see Sect. 2 for details), and thus, the very outskirts of the disc, for a sample with positions and velocities of excellent quality. Moreover, important improvements in the pipelines of the *Gaia* photometry have resulted in photometric bands with significantly less systematic error, from which, combined with the improved parallaxes, cleaner HR diagrams can be built and used to select different populations and components.

The paper illustrates how, once more, the new *Gaia* data are set to revolutionise our knowledge of the Galaxy and its past. Additionally, we describe practical aspects of the data and examples of its use that might be of interest for the community, such as queries in the *Gaia* Archive, quality cuts, derivation of distances (Bayesian inference, considerations on the parallax zero point), etc. We also complement our analysis with the use of simulated data from the *Gaia* Object Generator (GOG, Luri et al. 2014) and the *Gaia* Universe Model Snapshot (GUMS, Robin et al. 2012), now available directly in the *Gaia* Archive, to evaluate the effects of selection, errors and extinction.

We start our paper by explaining the different datasets used and demonstrating the different improvements (but also limitations) of the EDR3 data in the anticentre direction (Sect. 2). We continue by explaining how the distances and phase space coordinates are derived (Sect. 3). The results sections follow, organised into the explorations of the disc dynamics (Sect. 4), halo, thick disc and outer disc structures (Sect. 5), and distant

open clusters (Sect. 6). We present our discussion and conclude in Sect. 7.

2. Data

2.1. Main datasets

In this work we explore the Galactic anticentre region using different data selections obtained from *Gaia* EDR3 (Gaia Collaboration 2021a) that can be accessed through the *Gaia* Archive¹. More details on the data and validation are given also in Lindegren et al. (2021b), Riello et al. (2021) and Fabricius et al. (2021). The main datasets are shown in Fig. 1 and listed below. The number of stars for these samples and a comparison with DR2 are in Table 1.

1. AC20: a square on the sky centred at $(\ell, b) = (180, 0)$ deg of 20 deg on a side (blue square in Fig. 1). This sample is used to explore Galactic disc kinematics in Sect. 4. It contains 14 120 029 stars but most of the time we use only the selection with $\varpi/\sigma_\varpi > 3$ (see Sect. 3.2), which comprises 3 518 388 sources (AC20- $\varpi/\sigma_\varpi > 3$). The data were retrieved from the archive using the query 1 in Appendix A. Similar queries were used for other samples.
2. ACV: a rectangle on the sky centred at $(\ell, b) = (180, 0)$ deg with a width of 20 deg in ℓ and height 100 deg in b (green rectangle in Fig. 1). This sample is used to explore the halo and the structures in the outer disc such as Monoceros or the Sagittarius stream in Sect. 5. For parts of our analysis, we performed a selection of $\varpi < 0.1$ mas to favour distant stars. We note that with this selection there are 2% fewer stars in EDR3 than in DR2 (Table 1). While the total number of stars in that region has increased with respect to DR2, many of the stars added are nearby faint dwarfs (see Sect. 2.3) and the overall quality of the parallaxes has improved significantly as proven by the decrease in the number of sources with a negative parallax (and spurious sources). As a consequence, our parallax cut is now able to reject the nearby sources more efficiently, thus resulting in a slightly smaller sample.
3. Two clusters in the anticentre. All sources brighter than $G = 19$ within 4 arcmin of the centres of the extremely distant Galactic old open clusters Berkeley 29 and Saurer 1. These data are analysed in Sect. 6.

In all our analysis, our fundamental observables are the astrometric quantities ϖ , μ_{α^*} , μ_δ (parallax and proper motions) and the photometric bands G , BP, RP. In order to use the best quality data, we applied several selections. First we applied the following astrometric quality selection on the Renormalised Unit Weight Error (RUWE) as recommended in Lindegren et al. (2021a):

$$\text{RUWE} < 1.4. \quad (1)$$

On the other hand, whenever the photometry was used we selected good photometry sources with:

$$\begin{aligned} 0.001 + 0.039(\text{BP} - \text{RP}) &< \log_{10} \text{ excess_flux} \\ &< 0.12 + 0.039(\text{BP} - \text{RP}). \end{aligned} \quad (2)$$

Sources out of these limits have inconsistent G , G_{BP} and G_{RP} fluxes due to blends (more than one source in the BP and RP windows), contamination by a nearby source (outside the window) or a sign of the extended nature of the source. Additionally, we corrected the fluxes in G for 6p sources following Riello et al.

¹ <https://gea.esac.esa.int/archive/>

Table 1. Number of stars in the different samples and comparison with DR2.

	DR2	EDR3	EDR3+filters
1. AC20	13 307 312	14 120 029	11 949 642
5p-6p ^(a)	10 750 864	12 279 076	11 949 642
$\varpi/\sigma_\varpi > 3$	2 645 014	3 518 388	3 369 456
photometry	12 618 364	13 706 954	11 436 625
2. ACV	24 578 296	25 835 286	21 835 927
$\varpi < 0.1$ mas	4 974 104	4 879 087	4 509 263
$\varpi < 0$ mas	3 945 985	3 781 306	3 496 645
3. Clusters			
Berkeley 29	365	370	334
Saurer 1	283	284	263

Notes. The numbers are given for the different data samples described in Sect. 2.2 and different sub-selections. The numbers in the first two numerical columns are for samples without the `excess_flux` and `RUWE` selections since these are not equally defined in the different releases. ^(a)See footnote 2.

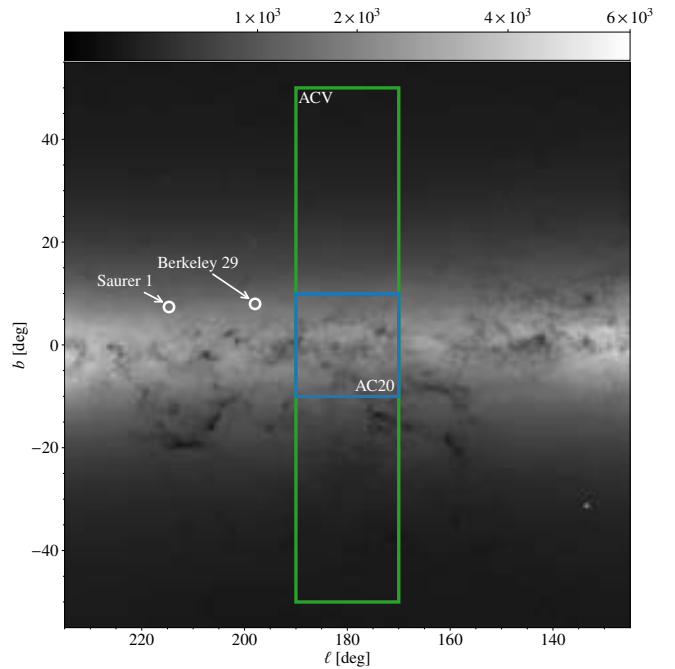


Fig. 1. EDR3 star counts in the anticentre region with the different data selections used. The HEALpix map is obtained by querying the *Gaia* archive the counts of stars within each HEALpix of level 8 (query 2 in Appendix A). The size of the circles to indicate the position of the clusters does not correspond to the size used for the selection which is much smaller. Several other clusters can be seen in the figure, and also the Triangulum Galaxy (M33, bottom right corner).

(2021) – their Table 5 – using directly an ADQL query as suggested in Gaia Collaboration (2021a). The last column in Table 1 indicates the number of stars after these selections.

2.2. Complementary datasets

For validation and other purposes, we also used the following complementary data:

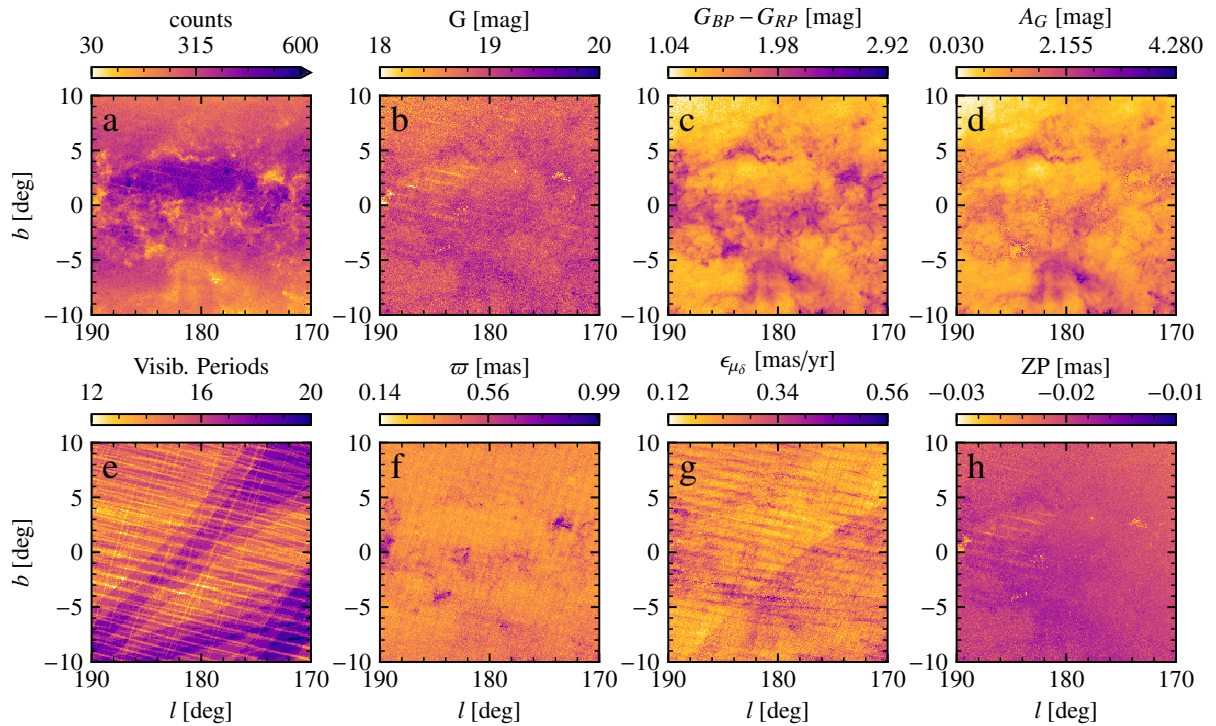


Fig. 2. Characteristics of the anticentre AC20 sky. *Panel a:* number of sources and the rest of panels show median quantities for bins of 0.1 deg of the magnitude (*b*), colour (*c*), extinction in the *G* band (*d*, only for stars with $w/\sigma_w > 3$, see Sect. 2.4), visibility_periods_used (*e*), parallax (*f*), uncertainty in the proper motion in the δ direction (*g*), and zero point correction to the parallax ZP_{56} (*h*, see Sect. 3.1).

- i. 6Dsample: a full sky sample with stars that have DR2 line-of-sight velocity in EDR3 (Seabroke et al. 2021), thus with full 6D phase space information. After filtering, this sample contains 6 156 684 stars and is used mainly in Sect. 4.
- ii. DR2: the same selections as above (AC20, ACV) but for DR2. These are used for comparison with EDR3.
- iii. GOG & GUMS: the same selections as above but for GOG (Luri et al. 2014; GEDR3 documentation Chapter 2) which is a mock *Gaia* catalogue based on the Besançon model (Robin et al. 2003), and for GUMS (Robin et al. 2012) which contains the intrinsic properties of the mock sources before applying the *Gaia* instrument modelling. Here we used the GOG version 20.0.3. with uncertainties that have been scaled to 34 months of data (but see Fig. E.1). These samples are used for the evaluation of completeness and extinction effects and they do not contain any kinematic sub-structure or asymmetries. Furthermore, GOG and GUMS were used in Appendix C for testing how robust each of the distance estimation methods is. These simulated data were retrieved through the *Gaia* Archive querying from the corresponding tables (`gaiaedr3.gaia_source_simulation` and `gaiaedr3.gaia_universe_model`).
- iv. 2MASS: we used the official crossmatch of EDR3 with the 2MASS point source catalogue (Skrutskie et al. 2006), provided in `gaiaedr3.tmass_psc_xsc_best_neighbour`. For the AC20 sample, this yields about 55% anticentre objects with 2MASS photometry. These data were used to select red clump (RC) stars and compute their photometric distances (Sects. 2.4 and 3.2, Appendices B and C.2.1).

2.3. EDR3 data quality and completeness

In this section we examine the quality of the EDR3 data and compare it to DR2. The most relevant improvements in EDR3

for our study include a larger number of sources at the faintest magnitudes and a significant decrease of the astrometric uncertainties and thus a significantly larger number of stars with a certain parallax precision. Below we show these aspects in more detail focusing mostly on the AC20 region as an example.

2.3.1. General description

Figure 2 shows the AC20 region in Galactic coordinates coloured according to different quantities in bins of 0.1 deg. In panel a we show the number of stars per bin while the rest of the panels show median quantities. As expected, the counts anti-correlate with the patterns seen in the extinction map from Green et al. (2019) (d, see details in Sect. 2.4) combined with the decrease with Galactic latitude $|b|$. The median magnitude (b) and median colour (c) also correlate with extinction (d): higher extinction regions have, on average, more reddened sources that have fainter (more extinguished) apparent magnitudes. Panel d shows that there is higher extinction for $b < 0$. Additionally, there is a horizontal elongated window at $b \sim 2.5$ deg of low extinction with far more counts and brighter magnitudes, which is seen also in other panels where brighter magnitudes essentially translate into smaller astrometric errors (e.g. panel g) and also smaller parallaxes (panel f, stars reaching farther distances). Whether this feature with larger counts reflects more than simply lower extinction (e.g. a flexing of the disc) requires a deeper analysis of the extinction and the selection function. We also note that the thin nearly-horizontal lines in panels a and b are a consequence of the RUWE selection.

2.3.2. Completeness

The evaluation of the completeness of the *Gaia* data is a difficult task given that there is no deeper survey with a comparable

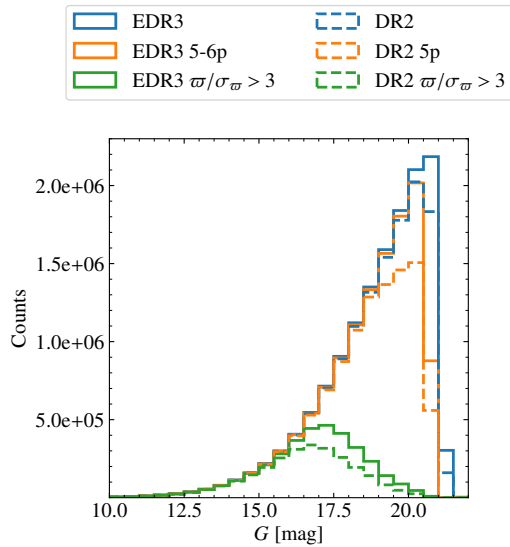


Fig. 3. Distribution of G magnitude in the anticentre. We show the number of stars in bins 0.5 mag for the AC20 case. The gain from DR2 to EDR3 is mostly at the faintest magnitudes where some sources did not have enough observations to appear in the past release.

resolution. Distinct methodologies to assess the data completeness can be found in Boubert & Everall (2020), Lindegren et al. (2021b) and Fabricius et al. (2021). Here we examine it in a simpler way. First we note that the AC20 sample (without any cuts) has about one million more stars in EDR3 compared to DR2 (see Table 1). Figure 3 shows histograms of the G magnitude for stars in the AC20 sample in DR2 and EDR3 (blue solid and dashed histograms) showing a great increase in the number of sources at the faint magnitudes with respect to DR2. This was expected given that the detection on board prioritises bright magnitudes and the effect of more months of observations produces new detections mostly at the faintest bins.

Figure 2e shows the map of median `visibility_periods_used`. This panel shows bands at different spatial scales that correspond to regions with higher and lower number of observations and thus higher and lower completeness, respectively. The thin, nearly-horizontal, yellowish pattern, separated by roughly 0.7deg, similar to the width (across scan) of *Gaia*'s FOV, corresponds to consecutive scans that did not overlap in across scan. The wider purple bands, indicating areas where the coverage is better, are close to some ‘nodes’ in the scanning law, that is, the positions in the sky that get repeated coverage during some consecutive scans. Figure 4 shows the star counts for different ranges in G for DR2 (top) and EDR3 (bottom) using the same colour scale. The bands of the scanning law appear clearly and correlate with Fig. 2e. Comparing to DR2, we can clearly notice the larger number of stars in EDR3 in these two magnitude ranges as well as the reduction of some of the bands (at scales of ~ 3 deg) imprinted in DR2. In the range of $20.75 < G < 21$ some scanning bands are still present.

2.3.3. Completeness of the kinematic samples

Some of the *Gaia* sources have only partial astrometric solutions, from which only sky coordinates are derived (2p solutions) while others have full astrometric solution (positions, parallax and proper motions available) and are dubbed 5p and 6p solutions (Lindegren et al. 2021b), where the 6th parameter is the

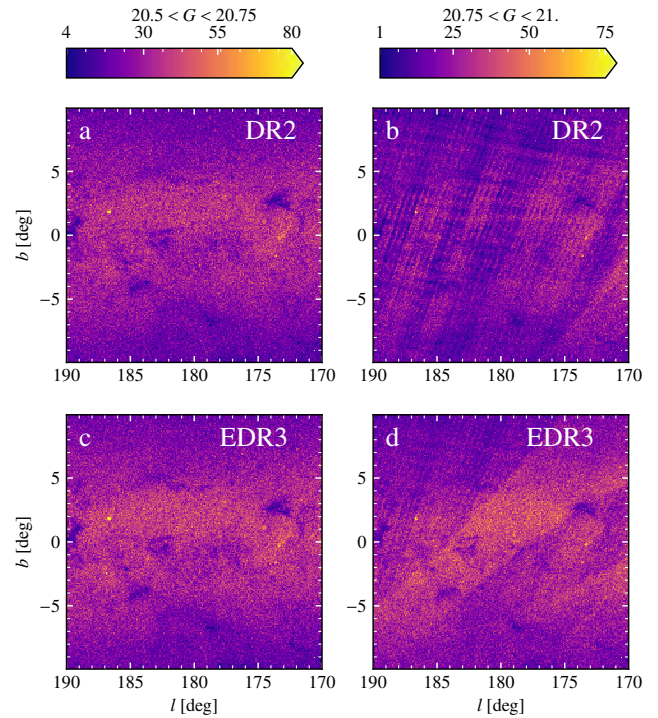


Fig. 4. DR2 and EDR3 counts for different magnitude ranges. The panels show the number of sources in bins of 0.1 deg in two different ranges of magnitude: $20.5 < G < 20.75$ (left) and $20.75 < G < 21$. (right). To facilitate the comparison, the same colour bars has been used for each vertical pair of panels and the upper limit of the colour scale does not correspond to the maximum number of counts to avoid dominance of bins with clusters. An increase in the counts in EDR3 is observed, together with the decrease of some of the small scale patterns, although some bands remain in the faintest magnitude range.

colour². In the first rows of Table 2 we give the number of stars with partial (2p) and full (5p, 6p) solutions comparing DR2 and EDR3 for the whole AC20 sample and for different ranges of magnitude. In EDR3, there are two million more stars with full astrometric solution than in DR2. The table also shows the percentage of full solutions relative to all sources in EDR3, which gives an indication of the internal completeness of the kinematic data. Most notably, in the range of $19 < G < 20$ there is now a 98% internal completeness compared to the 82% in DR2, and in the range $20 < G < 20.7$ the percentage is now 90% versus the old 64%, verifying that, as shown also with the orange solid and dashed histograms of Fig. 3, there is an outstanding gain at the faintest magnitudes. These stars have never been used before in kinematic studies with *Gaia* data.

We note that 6p solutions tend to be associated to fainter sources and their astrometric solutions are worse than for 5p ones. They have on average fewer `visibility_periods_used` (i.e. less observations), and larger `ipd_frac_multi_peak` (i.e.

² 2p partial solutions (only positions) are indicated as `astrometric_params_solved=3` in the *Gaia* Archive. 5p solutions are those for which the *Gaia* colour is used in the astrometric solution, while in the 6p cases, this quantity, more precisely, the pseudocolour, is derived simultaneously in the solution (Lindegren et al. 2021b). The 5p and 6p solutions correspond to `astrometric_params_solved=31` and 95, respectively. In DR2 all full astrometric solutions were included under the `astrometric_params_solved=31` case, even if in some cases a chromaticity different from the photometric colour was used.

Table 2. Indicative completeness of the kinematic samples.

	DR2			EDR3			
	2p	5p	5p /ALL-EDR3	2p	(5p∪6p)	(5p∪6p) /ALL-EDR3	
$\forall G$	2 5564 48	10 750 864	76%	1 840 953	12 279 076		87%
$G < 19$	111 638	5 860 281	96%	67 217	6 010 199		99%
$19 < G < 20$	492 849	2 825 129	82%	60 360	3 369 371		98%
$20 < G < 20.7$	940 298	1944 641	64%	312 553	2 705 704		90%
	$\varpi/\sigma_\varpi < 3$	$\varpi/\sigma_\varpi > 3$	$\varpi/\sigma_\varpi > 3$ /ALL-EDR3	$\varpi/\sigma_\varpi < 3$	$\varpi/\sigma_\varpi > 3$	$\varpi/\sigma_\varpi > 3$ /ALL-EDR3	
$\forall G$	10 662 298	2 645 014	19%	10 601 641	3 518 388		25%
$G < 15$	30 930	478 565	93%	13 098	500 913		97%
$15 < G < 17$	360 149	1 096 109	74%	170 528	1 301 329		88%
$17 < G < 19$	6 284 445	1 039 701	14%	5 860 892	1 660 388		22%
$19 < G < 21$	3 826 133	30 637	0.7%	4 232 117	55 142		1%

Notes. Absolute number of stars and fractions for all magnitudes and for distinct magnitude ranges are given for the cases with 2p and 5-6p solutions and for the selection of $\varpi/\sigma_\varpi > 3$. To compute the percentages for DR2, the total number of sources in EDR3 for each case has been used. These numbers are for samples without the `excess_flux` and `RUWE` selections since these are not equally defined in the different releases and the selection in `RUWE` eliminates the 2p solutions.

relatively large probability of being a double source, either visual or real binary), having larger astrometric errors. While for the AC20 sample the fraction of 6p solutions is comparable to the 5p (42 and 45%, respectively, the remaining 13% being 2p), for the AC20- $\varpi/\sigma_\varpi > 3$ case they represent only a 14% (86% being 5p) since we require good relative parallax errors.

After selecting stars with $\varpi/\sigma_\varpi > 3$ (AC20- $\varpi/\sigma_\varpi > 3$ sample) we find approximately one million more stars in EDR3 than in DR2 (bottom rows of Table 2), which represents an increase of 33%. Figure 3 (green solid and dashed histograms) shows an improvement of the completeness of the parallax quality selection at magnitudes fainter than $G = 16$, which means better sampling at all distances and probing larger ones. Table 2 also shows that at the relatively bright magnitudes $15 < G < 17$, there were 74% of stars in DR2 satisfying this condition but we have now 88%. It is nevertheless important to remark that the completeness of the sample with good parallaxes is low even at intermediate magnitude ranges both for the DR2 and EDR3 (as low as 14 and 22% in the range $17 < G < 19$, respectively), although we see an overall improvement for the new release.

2.3.4. Astrometric quality, systematics and parallax zero point

The improvement in astrometric quality of EDR3 with respect to DR2 is discussed in Lindegren et al. (2021b) and is reflected in smaller uncertainties and a reduction of the number of negative parallaxes (e.g. for the ACV sample where there are 164 679 less sources with negative parallaxes, Table 1). Figure E.1 illustrates the improvement in the uncertainties for the anticentre (similar to Fig. A.1 by Lindegren et al. 2021b for all EDR3). There is a reduction by a factor of 0.79 and 0.5 in parallax and proper motion uncertainties, respectively, as expected for the increase in the number of months of observations, and even a larger reduction for sources with $G < 14$. This improvement in the astrometric quality allows us to have now a much larger sample of stars with very good relative parallax errors, and reach farther distances from the Sun. We also note that the uncertainty in μ_δ is smaller than for μ_{α^*} . This is due to a geometrical scaling factor on the uncertainties resulting from the scanning law which in the direction of the anticentre favours μ_δ .

As in previous releases, the astrometric *Gaia* data suffer from some systematics. The median astrometric quantities and

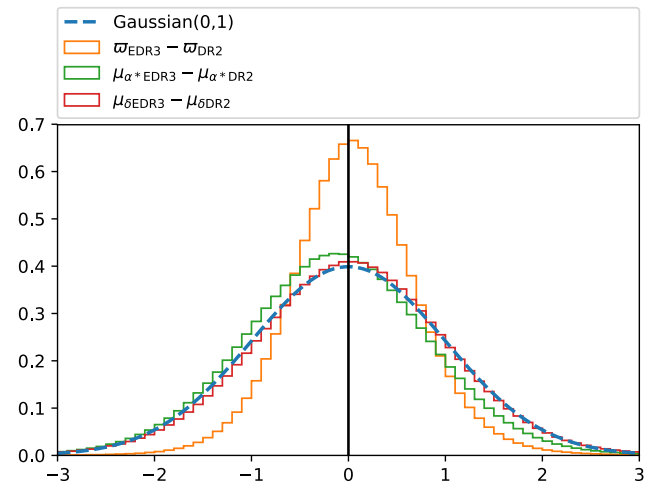


Fig. 5. Consistency between astrometric values in DR2 and EDR3. The histograms show the differences in parallax and proper motion normalised to the errors $(x_{\text{EDR3}} - x_{\text{DR2}}) / \sqrt{\sigma_{x,\text{EDR3}}^2 + \sigma_{x,\text{DR2}}^2}$, where x is ϖ , μ_{α^*} or μ_δ , and compared to a Gaussian distribution with 0 mean and variance of 1. The differences in μ_{α^*} are due to a systematic in DR2 that has been now corrected. We have corrected the parallaxes (Eq. (3)) using the median offset for DR2 ($-27 \mu\text{as}$) and for EDR3 ($-17 \mu\text{as}$).

their uncertainties show checkered patterns that somehow correlate with the scanning law, as illustrated for the median parallax (Fig. 2f) and median uncertainty in μ_δ (Fig. 2g). The later shows additionally some of the large scale bands mentioned above. The amplitude of these systematics has, however, been reduced in EDR3 (see Lindegren et al. 2021b). Another known systematic is a zero point in parallax Lindegren et al. (2021a) that has also been reduced and which we examine in detail in Sect. 3.1.

Figure 5 shows the differences in all astrometric quantities between DR2 and EDR3 normalised to the errors³. The median absolute differences between EDR3 and DR2 are $15 \mu\text{as yr}^{-1}$ in ϖ , $-48 \mu\text{as yr}^{-1}$ in μ_{α^*} and $7 \mu\text{as yr}^{-1}$ in μ_δ . For comparison,

³ We have used the `gaiaedr3.dr2_neighbourhood` table for the correspondence between sources.

we show a Gaussian distribution with 0 mean and 1 as variance with a blue curve, although the quantities from DR2 and EDR3 are not independent and thus these distributions are not expected necessarily to follow this curve. The large systematic differences in μ_{α^*} (green histogram) is explained by a correction of the reference frame (spin) for EDR3 that has largely reduced the medium-scale (1–20 deg) inhomogeneities in the median parallax and proper motion of the quasars, which actually were quite large precisely in the direction of the anticentre for μ_{α^*} (about $0.1 \mu\text{as}$, Fig. 13 of Lindegren et al. 2021b). The histogram of parallax differences is narrower than the Gaussian case and is slightly positively biased. In Fig. 5 the zero point has been corrected using the median estimated values for quasars respectively in DR2 and EDR3 (more details are given in Sect. 3.1). We note that the bias was even larger if we neglected the corrections (giving a median of $25 \mu\text{as}$). The persistent bias after the correction could be attributed to underestimation of the zero point in DR2 (for which there is some evidence, see Lindegren et al. 2021a) or effects of considering a fixed value of the offset (Sect. 3.1).

2.3.5. Photometric quality

The improvement of the photometry of EDR3 with respect to DR2 is described in Riello et al. (2021). In summary, the increase in the number of observations and the improvement of several steps of the pipelines (image parameter determination, LSF and PSF calibrations, cross-match and photometry) have led to a significant decrease of the systematics at the bright end ($G < 15$). The effects of blends and contamination by nearby stars are mainly filtered out using Eq. (2).

2.4. Extinction and selection of tracer populations

We used two different approaches to select the tracer populations. The first one uses only *Gaia* data and the populations were selected in the de-reddened HR diagram. In the second approach, external photometric data were used to define a sample of RC sources.

2.4.1. Method I: using the *Gaia* HR diagram

We obtained the de-reddened HR diagram for the AC20- $\varpi/\sigma_\varpi > 3$ sample using the 3D dust-reddening maps from Bayestar (Green et al. 2019). We used the d_{PM} distances (Sect. 3.2 and Appendix C.1) and the galactic (ℓ, b) coordinates to infer the line-of-sight visual extinction A_V for each source. Then we transformed A_V to A_G and $E(BP - RP)$ using the *Gaia* extinction factor from Casagrande & VandenBerg (2018). We compared our results with the ones using the extinction model by Lallement et al. (2019) and the conversion to A_G and $E(BP - RP)$ following Appendix A in Ramos et al. (2020), finding only mild differences in the classification of stars without consequences on the conclusions from the subsequent sections.

Figure 6 shows the *Gaia* de-reddened HR diagram for the AC20- $\varpi/\sigma_\varpi > 3$ sample. We used the direction of the extinction line in this diagram ($M_G = 1.95(BP - RP)_o - 0.8$, black diagonal line) combined with the vertical cut $(BP - RP)_o > 0.65$ to select (conservatively) giants (purple dots). Then we used the PARSEC isochrones (Bressan et al. 2012; Marigo et al. 2017) and respective updates⁴ to perform a statistical partition by ages of the main sequence sources into extremely young (EYP, 0.2 Gyr), young (YP, 0.2–2 Gyr), intermediate (IP, 2–8 Gyr) and

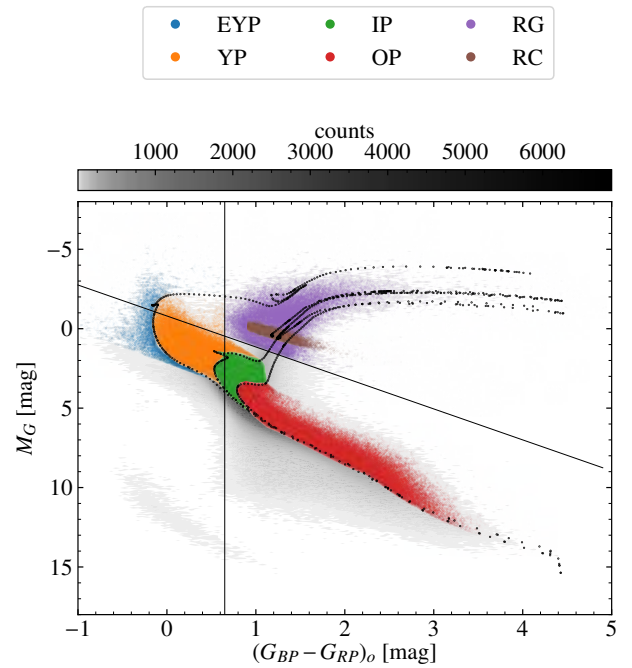


Fig. 6. De-reddened HR diagram of the anticentre region and different selected populations. The diagram is shown for the 3 369 456 sources of the AC20- $\varpi/\sigma_\varpi > 3$ sample with available photometry (G, BP, RP) and extinction data and absolute magnitudes derived considering the d_{PM} distances. We over-plot three PARSEC stellar isochrones with $[M/H] = 0$ for the ages of 0.2, 2 and 8 Gyr, a line at $BP - RP = 0.65$ and a diagonal line following the extinction slope used for the selection of populations (Method I) which appear in different colours. The RC have been selected using a different method (Method II).

Table 3. Populations in the AC20 sample.

Population	Sources
All	3 369 456
EYP Extremely young massive ($\tau \lesssim 0.2$ Gyr)	12 792
YP Young main sequence with $0.2 \lesssim \tau \lesssim 2$ Gyr	276 344
IP Intermediate main sequence with $2 \lesssim \tau \lesssim 8$ Gyr	807 910
OP Old main sequence	1 032 916
RG Red giants	176 193
RC Red clump	121 857

Notes. The selections are obtained following the Method I, except for the RC of the last row (Method II).

old populations (OP), as specified in Table 3 and illustrated in Fig. 6. The massive sources of the EYP were constrained to have $(BP - RP)_o < 0.65$, while the YP, IP and OP were selected between the lower (ZAMS) and the upper (TAMS) luminosity boundary of the main sequence band defined by the PARSEC stellar evolutionary tracks at $[M/H] = 0$. We note that while the OP has contribution from young stars, we can claim it is on average older than the IP: we expect an average age of 4–5 Gyr (e.g. Fig. 13 in Bland-Hawthorn et al. 2019) but with an important contribution of the oldest stars in the disc. In general, these selections are contaminated by stars of different ages due to several aspects (stars with different metallicities to the ones used in the isochrones, inaccuracies of the extinction model used,

⁴ <http://stev.oapd.inaf.it/cgi-bin/cmd>

confluence of isochrones around the ZAMS, binarity, etc). Nevertheless, we expect our samples to be dominated by the age ranges desired, which is enough for our basic purposes here.

2.4.2. Method II: using *Gaia* and 2MASS

We combined EDR3 parallaxes and *G*-band photometry with that from 2MASS *K*-band for the AC20 sample. The passbands in 2MASS are narrow and in the infrared, and are thus weakly affected by errors in the extinction estimation. For 2MASS, the flag (qfl) = ‘AAA’ indicates the highest photometric quality. However, this would significantly reduce our sample (to only 15% of the entire AC20 sample). Instead, we chose to enforce a quality cut only at the distance estimation stage using the photometric errors, e_{jmag} & e_{kmag} . We first computed the extinction of each source using the 3D dust-reddening maps from Bayestar (Green et al. 2019) with the inverse of the parallax as a prior for distance. The RC sources were selected in a Bayesian manner around the literature values for the absolute magnitude of the RC simultaneously for the *G* *Gaia* band and the 2MASS *K* band. We compared these distances with the ones using Bayesian distances for the prior (d_{PM} , see Sect. 3.2) and our results do not change significantly. More details of the procedure and a validation with an external sample are given in Appendices B and C.2.1.

3. Distances and phase space coordinates

In this section we describe how the distances and phase coordinates are computed in our study. We start by discussing the zero point in the *Gaia* parallaxes (Sect. 3.1), which needs to be corrected in order to estimate first distances (Sect. 3.2), and subsequently Galactic cylindrical positions and velocities (Sect. 3.3).

3.1. Parallax zero-point correction

As for previous releases, the *Gaia* parallaxes have a zero point⁵ (ZP) that needs to be considered. In EDR3 the median parallax of the quasars is $-17\ \mu\text{as}$ (Lindegren et al. 2021a). This negative correction needs to be subtracted from the EDR3 parallaxes (parallaxes need to be increased by $\sim 17\ \mu\text{as}$):

$$\varpi^{\text{corrected}} = \varpi - \text{ZP}, \quad (3)$$

or equivalently, reducing the inferred distance. Here we corrected all parallaxes by subtracting $\text{ZP} = -17\ \mu\text{as}$. Additionally, when relevant, we also compared our results with the more sophisticated approach presented in Lindegren et al. (2021a). In that work, they estimate the parallax zero-point ZP_{56} as a function of magnitude, colour (more precisely, `nu_eff_used_in_astrometry` for the 5p solutions and `pseudocolour` for the 6p solutions, hence the names ZP_5 and ZP_6), and ecliptic latitude, by looking at the parallaxes of quasars, binary stars and sources in the Large Magellanic Cloud for EDR3. Here we computed ZP_{56} using the Python implementation that is available online as part of the *Gaia* EDR3 access facilities⁶. Panel h in Fig. 2 shows the median zero-point ZP_{56} in the AC20 region. We observe a mild dependency of its value on the sky position. The median value for all stars

in AC20 region is $\text{ZP}_{56} = -20\ \mu\text{as}$, thus similar to that of the quasars, with the 10 and 90 percentiles being -32 and $-14\ \mu\text{as}$, respectively, and $\text{ZP}_{56} > 0$ only for 0.02% of the stars. For the $\text{AC20-}\varpi/\sigma_{\varpi} > 3$ sample, which has a significantly different magnitude distribution compared to the case without the parallax quality cut (Fig. 3), we find a median ZP_{56} of $-30\ \mu\text{as}$ and percentiles of -38 and $-20\ \mu\text{as}$, respectively. The ZP_{56} case, thus, yields the largest differences between uncorrected and corrected distances (Fig. D.1). The velocities, which depend linearly on the distances, are consequently scaled as well. All these will be important in order to determine, for example, the exact distances to some kinematic features that we detect but we do not observe any qualitative difference in our results. More details are given in Appendix D and throughout the paper.

3.2. Distances

To convert the astrometric measurements by *Gaia* into phase space coordinates, we require an estimate of the distance to a given star. The complications of estimating distances to stars given their measured parallaxes have been discussed by a number of authors over a long period of time (e.g. Strömberg 1927; Lutz & Kelker 1973; Bailer-Jones 2015; Luri et al. 2018). The transformation between parallax and distance is non-linear, which leads to a number of issues, including the extreme case of negative measured parallaxes. Simply taking the inverse of the measured parallax gives a biased estimate of the distance of a star, and this bias grows more serious as the relative uncertainty grows larger. It has therefore become extremely common to apply a Bayesian approach to the problem of providing distance estimates from parallaxes, and/or to use photometric information to produce a better estimate of the distance.

We work primarily with distance estimates from a Bayesian approach (d_{PM}), similar to that applied by Schönrich & Aumer (2017), with a prior that is derived iteratively to be consistent with the data. These distances use a prior $P(d) \propto d^2 P_{\rho}(r(d)) S(d)$, where $r(d)$ is the position at distance d along a given line-of-sight, so $P_{\rho}(r(d))$ is proportional to the density of a model Galaxy. The term $S(d)$ is the selection function – i.e. the probability that a randomly chosen star at a distance d enters the catalogue. The distance estimate, \bar{d} is then found as the expectation value of d given this prior and the measured parallax (and its uncertainty). As explained in the previous section, default distances are computed considering a fixed parallax zero point of $-17\ \mu\text{as}$.⁷ More details can be found in Appendix C.

To check that our results are robust, we compared to results when we estimate the distance as simply the inverse of the parallax, and also with a different Bayesian approach based on that from Bailer-Jones et al. (2018). We tested each of these approaches on GOG data, and further details are given in Appendix C. From these tests, we conclude that using a parallax quality cut of $\varpi/\sigma_{\varpi} > 3$ is a good compromise between the performance of the estimate and the number of stars of our samples. However, we emphasise that all the estimators tested here return somehow imperfect distances, which in the Bayesian case depend also on how close the assumed prior on the Galaxy distribution is to the Galaxy model used in GOG (i.e. the Besançon Galaxy Model). We find that the median relative difference between the simulated true distances and the estimated ones can be as large as 20% at 4 kpc and larger than 50% for 25% of the stars even with the $\varpi/\sigma_{\varpi} > 3$ selection.

⁵ We use a different notation compared to Lindegren et al. (2021a) to distinguish with the vertical cylindrical coordinate Z .

⁶ https://gitlab.com/icc-ub/public/gaiadr3_zeropoint

⁷ The distances and the code can be found at <https://zenodo.org/record/4415706> and <https://zenodo.org/record/4415669>, respectively.

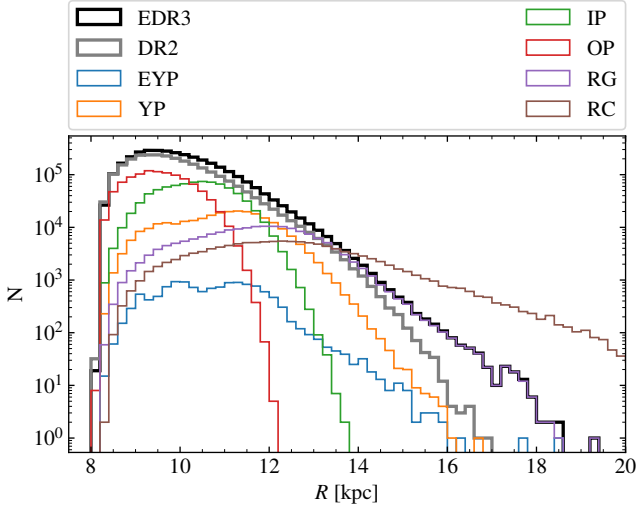


Fig. 7. Distribution of stars in Galactocentric radius. Number of stars per radial bin of 200 pc for the whole AC20- $\varpi/\sigma_\varpi > 3$ sample for EDR3 (black line) and DR2 (grey line), and for each stellar population (colour lines as indicated in the legend). The RC do not have the constraint $\varpi/\sigma_\varpi > 3$ and appears more extended in R than the black distribution.

On the other hand, for the stars classified as RC (see Sect. 2.4), we inferred their distance (d_{RC}) in a Bayesian manner using complementary photometric data from 2MASS (details are given in Appendix C.2.1). Typical uncertainties are of 1 kpc at a distance of 6 kpc (see Fig. C.5).

3.3. Positions and velocities

From the distances obtained in Sect. 3.2 and the sky positions, we computed the Galactic Cartesian (X, Y, Z) and cylindrical (R, ϕ, Z) positions, assuming that the Sun is located at $d_{\odot-GC} = 8.178$ kpc from the Galactic centre (GRAVITY Collaboration 2019) and a height above the Galactic plane of $Z_{\odot} = 0.0208$ kpc (Bennett & Bovy 2019). Figure E.2 shows the spatial distribution of the AC20 sample. By construction, the vertical Z and azimuthal Y distributions are wider for larger distances from the Sun, with some stars at $R \sim X = 14$ kpc reaching heights of 1 kpc above and below the plane. Figure 7 shows the number of stars as a function of Galactocentric radius. The gain in EDR3 for sources with $\varpi/\sigma_\varpi > 3$ (black line) compared to DR2 (grey line) at large radii is very significant with an increase of one order of magnitude already at 16 kpc and notably more stars at almost all radii.

For the different populations detailed in Sect. 6 (colour lines in Fig. 7), the samples with younger ages have distributions that, as expected, extend to larger radii compared to older populations. The distribution for the whole sample with $\varpi/\sigma_\varpi > 3$ is dominated by dwarfs for $R < 12$ kpc while giant stars take over beyond that. We see some hints of an over-density at around 12 kpc for the EYP and YP that could be the Perseus spiral arm but a good assessment of this requires more investigations of the selection function and the extinction. For the RC whose distances are computed photometrically without the $\varpi/\sigma_\varpi > 3$ constraint (brown line), there is a larger number of stars at large distances compared to the whole sample with $\varpi/\sigma_\varpi > 3$ (black line).

For the velocities, we computed V_ℓ and V_b and corrected them for the reflex of the solar motion using the following

equations:

$$V_\ell = kd\mu_\ell - U_\odot \sin(\ell) + (v_{c,\odot} + V_\odot) \cos(\ell) \quad (4)$$

$$V_b = kd\mu_b + [-U_\odot \cos(\ell) - (v_{c,\odot} + V_\odot) \sin(\ell)] \sin(b) + W_\odot \cos(b), \quad (5)$$

where $k = 4.7404705$ is the usual factor for units conversion, and we assume $U_\odot = 11.1$, $v_{c,\odot} + V_\odot = 248.5$, $W_\odot = 7.25$ km s⁻¹ for the solar motion (Schönrich et al. 2010; Reid & Brunthaler 2020), where $v_{c,\odot} \equiv v_c(R=R_\odot)$ is the value of the rotation curve at the Sun's position. In the anticentre direction, V_ℓ and V_b are approximately aligned with the usual cylindrical velocities V_ϕ and V_Z and, thus, we use:

$$V_\phi^* \equiv -V_\ell \quad (6)$$

$$V_Z^* \equiv V_b. \quad (7)$$

We note that V_ϕ^* is positive for most of the disc stars with this definition and that V_ϕ^* is not exactly equivalent to V_ϕ , nor is V_Z^* to V_Z , due to a geometric difference in the vector orientation and the contribution of the line-of-sight velocity, but the differences are small in the anticentre. In the Appendix E we used GOG to quantify this and we find that 80% of the sources with $\varpi/\sigma_\varpi > 3$ have absolute differences smaller than 2.9 and 3.3 km s⁻¹ for V_ϕ^* and V_Z^* , respectively (Figs. E.4, E.5 and E.3). We see that V_ϕ^* is mainly smaller than V_ϕ with a median of -0.4 km s⁻¹. When examining how these differences are distributed in the ℓ - b projection, we see, as expected, larger differences in V_ϕ^* the farther from the exact anticentre line ($\ell = 180$ deg). The differences in V_Z^* show a quadrupole symmetry, indicating that any kinematic signature following this same shape in the sky would be clearly suspicious but that for most of the cases, since we average over the whole area, the global effect of these differences is null. For stars in the *Gaia* 6D phase space sample (thus a more realistic case), the differences are similar though slightly larger (80% of the stars with $\varpi/\sigma_\varpi > 3$ have absolute differences smaller than 3.2 and 4.0 km s⁻¹ for V_ϕ^* and V_Z^* , respectively).

Another reference system for the velocities that we used in Sect. 5.1 is the tangential velocity V_t defined as:

$$V_t \equiv kd \sqrt{\mu_\alpha^2 + \mu_\delta^2}. \quad (8)$$

In particular for that section we used as distances the inverse of the parallax with a more strict selection of $\varpi/\sigma_\varpi > 5$.

We used the Jacobian matrix to compute the errors in the positions and velocities from the errors (and correlations) of the astrometric quantities. We neglected the errors in the angular positions since they are extremely small. In the case of the Bayesian and photometric distances, no correlation between distance d and proper motions μ was considered (but see discussion Appendix C). Figure 8 shows the median uncertainty in the radius R (top) and velocities (bottom) as a function of R for EDR3 (solid lines) for the AC20- $\varpi/\sigma_\varpi > 3$ sample, and the area delimited by the 25 and 75 percentiles (shaded regions). The median errors in R (solid blue line) remain lower than 1 kpc for $R < 14$ kpc and the velocity uncertainties (solid orange and green lines) are smaller than 5 and 2 km s⁻¹ for V_ϕ^* and V_Z^* , respectively, for most of the radii probed. The slight change of trend in the solid curves at around 12 kpc is due to the contributions of different stellar types, in particular giants stars that are intrinsically brighter at a given R and have, thus, smaller astrometric

Table 4. Uncertainties in phase space coordinates for the different *Gaia* releases.

	AC20- $\varpi/\sigma_\varpi > 3$					
	Median			80% of sources		
	ϵ_R	$\epsilon_{V_\phi^*}$	$\epsilon_{V_z^*}$	ϵ_R	$\epsilon_{V_\phi^*}$	$\epsilon_{V_z^*}$
DR2	0.30	3.8	2.2	<0.57	<8.4	<4.6
EDR3 (\cap DR2)	0.18	2.3	1.2	<0.42	<5.6	<3.0
EDR3	0.3	3.1	1.7	<0.58	<7.4	<3.9

	6dsample					
	Median $\epsilon_{v_{\text{los}}} = 0$			Median		
	ϵ_U	ϵ_V	ϵ_W	ϵ_U	ϵ_V	ϵ_W
DR2	0.09	0.09	0.07	0.43	0.44	0.38
EDR3	0.04	0.04	0.04	0.38	0.39	0.34

Notes. In the first rows we show the median uncertainties (first three numerical columns) and upper limit uncertainty for 80% of stars (three columns from the right) for stars in the AC20- $\varpi/\sigma_\varpi > 3$ sample for DR2 (first row), for the stars from EDR3 in common with DR2 (using the `gaiadr3.dr2_neighbourhood` table for the correspondence between sources), and for EDR3. The last rows compare the heliocentric velocity uncertainties in DR2 and EDR3 for the sample with 6D velocities (6dsample) when the error in v_{los} is not (left) and is considered (right).

uncertainties. Table 4 gives a summary of these position and velocity errors: 80% of stars have errors <0.6 kpc in Galactocentric radius, and <7 and <4 km s⁻¹, respectively for V_ϕ^* and V_z^* . The errors for V_z^* are smaller than for V_ϕ^* due to the better alignment of μ_b with μ_δ which in turn has smaller errors than μ_α in this sky direction as seen in Sect. 2.3 (Fig. E.1).

In Fig. 8 we also show the equivalent errors in DR2 (dashed lines). However, a fair comparison requires that we compare only the common sources (otherwise the new sources of fainter magnitudes in EDR3 at each bin in R contribute in a negative way to the overall values). The dotted lines obtained for the sources of EDR3 in common with DR2 show a quite significant improvement. For the velocities, the uncertainties are now smaller by about $\lesssim 2$ km s⁻¹ at a Galactocentric distance of $R = 12$ kpc, which represents an improvement of 30%.

Figure 9 shows the full error ellipses for a few stars chosen to sample different values of R in the R - V_ϕ^* projection that we explore later. While the black error bars show the errors on the individual quantities, the error ellipses show large correlations between these two variables. This correlation is induced by the coordinate transformations, which in both axes have an approximately linear dependency with the distance error. As expected, the ellipses are all oriented pointing towards the position and velocity of the Sun assumed (indicated with a black star).

Finally, another good illustration of the improvement in the astrometry is the comparison of the uncertainties in the heliocentric velocities U , V and W for the 6dsample in DR2 (Katz et al. 2019) and EDR3 (Seabroke et al. 2021), which is shown in the last three rows of Table 4. Assuming that there are no line-of-sight velocity uncertainties, the median uncertainties (left columns) are reduced by around 50% in EDR3. Including the line-of-sight velocity uncertainties (rightmost columns) does not show such a reduction, highlighting that the line-of-sight velocity uncertainties dominate. This will change in DR3 where these uncertainties are expected to decrease substantially and millions of additional sources will have line-of-sight velocity measurements for the first time.

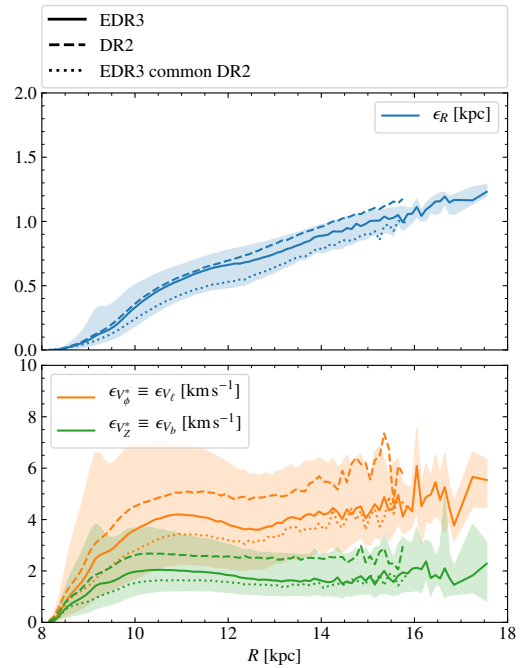


Fig. 8. Errors in phase space coordinates in the anticentre. The curves are for the AC20- $\varpi/\sigma_\varpi > 3$ sample and show the median errors for R (blue) in the *top panel*, and V_ϕ^* (orange) and V_z^* (green) in the *bottom panel*, while the shaded regions show areas enclosing 50% of the stars (that is, limited by the 25 and 75 percentiles). We show the values for EDR3 (solid), DR2 (dashed) and sources in common (dotted).

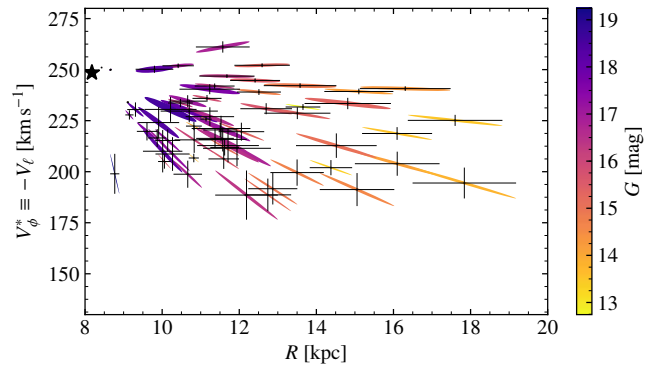


Fig. 9. Error ellipses in the R - V_ϕ^* plane for stars in the anticentre. The ellipses have been drawn for 60 stars from the AC20- $\varpi/\sigma_\varpi > 3$ sample chosen randomly but with weight of $\exp R$ in order to sample better the different R . The ellipses are coloured by magnitude G and the error bars are included as black lines. The error ellipses are oriented pointing towards the R_0 -($v_{c,\odot} + V_\odot$) point (black star).

4. Disc kinematics

In this section we explore the dynamics of the MW disc, analysing the velocities as a function of positions. As seen in Sects. 2.3 and 3.3, the improvement in the EDR3 astrometry allows us to probe the disc's outer regions. We start by examining the median velocities and velocity dispersions (Sect. 4.1) as a function of Galactocentric radius. We then look at large scale velocity asymmetries and phase space correlations in Sect. 4.2, to end with the analysis of small scale velocity substructures (Sect. 4.3) that are now resolved for the first time.

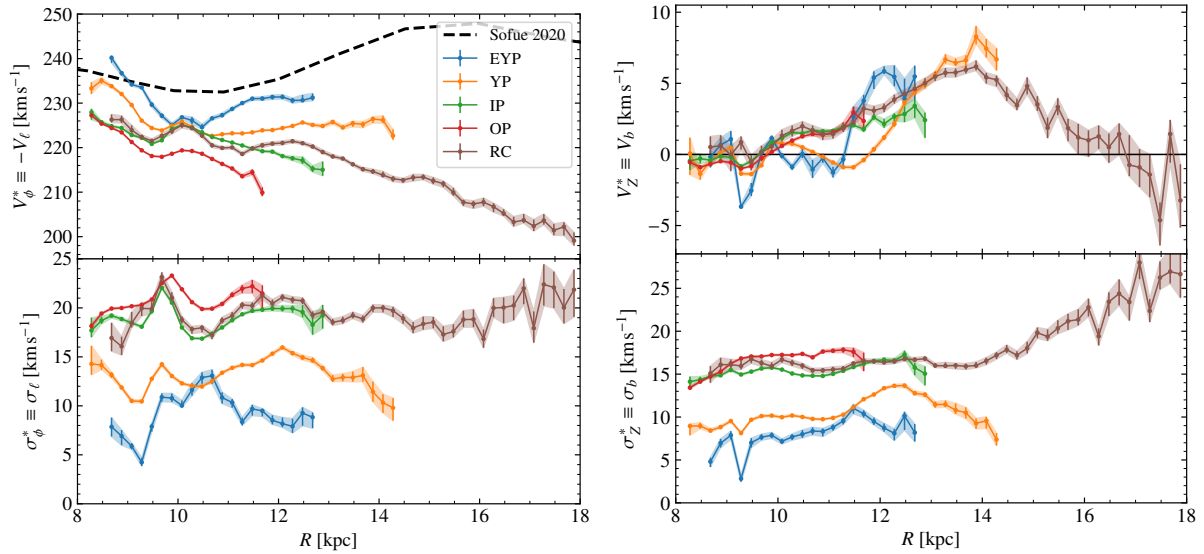


Fig. 10. Rotation and vertical velocity profiles in the anticentre. *Top:* median azimuthal and vertical velocities of the populations EYP, YP, IP, OP and RC as indicated in the legends (same as in Fig. 7). Shaded areas represent the uncertainties (see text) but they are very small and barely visible in most of the cases. The rotation curve by Sofue (2020) is over-plotted in the top left panel. *Bottom:* same as top but for the velocity dispersions (computed as 1.5MAD values). Apart from the expected differences due to the different ages of the populations and the asymmetric drift, we see significant oscillations in all curves.

4.1. Azimuthal and vertical velocities and dispersions

We measured the median velocity profiles and dispersions of V_ϕ^* and V_z^* for each stellar population. We used $\sigma^* \equiv 1.5\text{MAD}$ (where MAD is the median absolute deviation) as a robust estimate of the standard deviation, to which we subtracted the median error in each bin in quadrature. Using a robust estimator, rather than the standard deviation, prevents outliers from producing a noisy dispersion profile. Although the 1.5 factor is strictly valid only for normally distributed data, this approximation puts our values on the same scale as the standard deviation for a more easy comparison. We used bins of 200 pc and discard those with less than 100 stars. The uncertainties were then obtained by performing 1000 bootstrap resamplings of these distributions at each radius, choosing the 16th and 84th percentiles, and are indicated as shaded colour bands and error bars in the following panels.

The rotation velocity curves for the different populations are shown in the top left panel of Fig. 10. A difference in the median V_ϕ^* is observed for the different stellar populations with the older stars rotating slower as a result of the asymmetric drift. On average, the EYP stars rotate between 10 and $\sim 20 \text{ km s}^{-1}$ faster than the OP or the RC. The curve of the EY stars presents the best agreement with the rotation curve (black dashed lines) derived in Sofue (2020) from a compilation of kinematic data from molecular gas and stars in the infrared. This is consistent with the expectation that younger stars rotate as fast as the cold interstellar gas, thus at velocities closer to the true circular velocity of the MW. Globally, all the rotation curves decline for $R \lesssim 9.5 \text{ kpc}$ and show a bump at around 10 kpc. Beyond this, the curve of YP stars is flat, while those of older stars decrease again.

The effects of the parallax zero point are examined in Appendix D where we show, as an example, the effects of the different adopted values of this offset on the rotation curve of our $\text{AC20-}\varpi/\sigma_\varpi > 3$ sample (Fig. D.2). As expected and discussed in Sect. 3.1, we see slight differences in the curves due to a decrease of the distance and scaling of the velocities when the

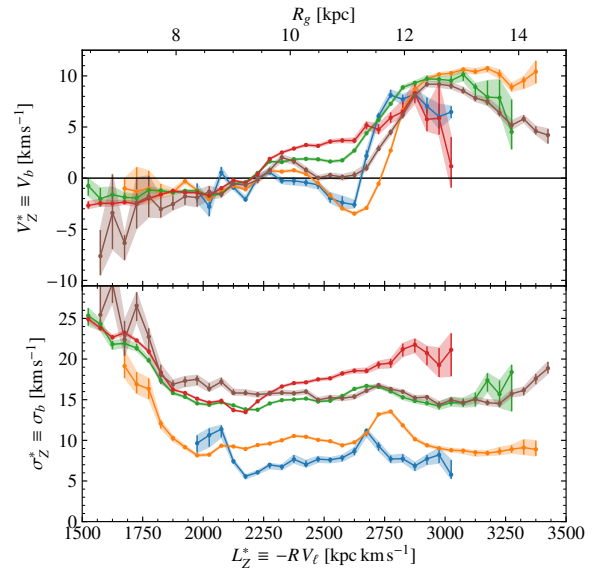


Fig. 11. Vertical velocity profiles as a function of angular momentum. The plot and legend is equivalent to the left panels of Fig. 7 but as a function of L_z^* . To guide the eye, we also show an approximate guiding radius $R_g = L_z^*/(236 \text{ km s}^{-1})$ on the top axis.

correction is used. However, the general features of the curves remain the same.

Interestingly, we observe stars from the YP rotating as far as 14.5 kpc from the Galactic centre. In total, we find as many as 1186 stars with $16 < R < 18 \text{ kpc}$ and $V_\phi^* > 200 \text{ km s}^{-1}$ for the $\text{ZP} = -17 \mu\text{as}$ (with median uncertainties of $\epsilon_R \sim 1. \text{kpc}$), and 275 for the case of ZP_{56} . This establishes a lower limit to the disc size although a detailed analysis is required, in particular in the context of the biases of the distance estimators, which can be large at these distances (see Fig. C.4).

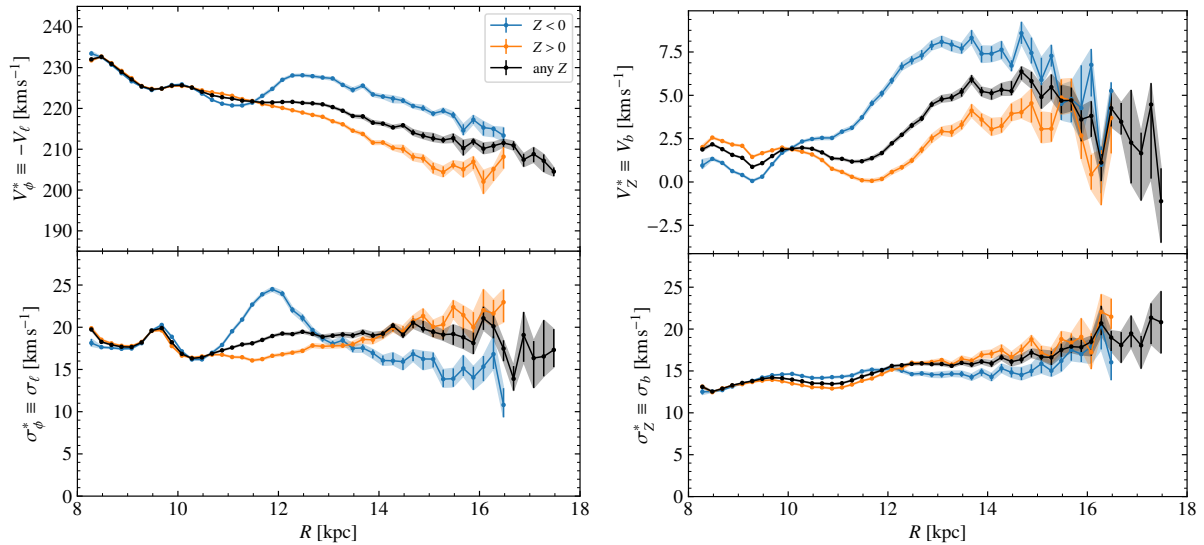


Fig. 12. Comparisons of the velocities above and below the Galactic plane. We plot the median azimuthal and vertical velocities (*top*) and velocity dispersions (computed as 1.5MAD values, *bottom*) for the whole sample $AC20-\varpi/\sigma_\varpi > 3$ (black lines, not including the sample of RC with photometrically derived distances), and for stars with $Z \geq 0$ (orange lines) and for $Z < 0$ stars (blue lines). Shaded areas represent the uncertainties. We observe notable asymmetries beyond 10–11 kpc.

The top right panel of Fig. 10 shows the median vertical velocities. These velocities appear to have small oscillations of the order of 2 km s^{-1} inside $R \sim 12$ kpc. There are clear dips at $R \sim 9.5$ kpc, coinciding with the dip in V_ϕ^* , and at $R \sim 11$ more prominent for the young stars. Figure 11 (top) shows the same velocities but as a function of L_z^* where the oscillations appear clearer with dips especially at around 2200 and $2600 \text{ km s}^{-1} \text{ kpc}$. In the later one, we can see a strong age dependence with younger populations showing a deeper valley. We note that at the extremes of L_z^* in this plot, the populations are biased towards high eccentricity orbits that are those that manage to reach the observed volume. Beyond the location of the dips, V_z^* increases and stars move in median upwards ($V_z^* > 0$). The profile of the RC stars with R (and of all populations in the L_z^* plot) draw a clear wiggle (with a subsequent decrease), with maxima of $\sim 5 \text{ km s}^{-1}$ at $R \sim 14$ kpc ($\sim 10 \text{ km s}^{-1}$ at $L_z^* \sim 3000 \text{ km s}^{-1} \text{ kpc}$). In Fig. 14 of Gaia Collaboration (2018c) only the first part of this positive vertical velocity wiggle was observed and seemed to have certain dependencies on the Galactic azimuth ϕ and vertical position Z of the stars, as we confirm in Sect. 4.2. The oscillations and the outer increase in the vertical velocities as a function of angular momentum were also observed in Schönrich & Dehnen (2018), Huang et al. (2018) and Cheng et al. (2020).

The bottom panels of Fig. 10 show the diversity in the velocity dispersions σ_ϕ^* and σ_z^* in the Galactic anticentre direction. Although we expect decreasing dispersions with R (van der Kruit & Freeman 1986, and references therein) supported by observations in external galaxies (Martinsson et al. 2013) including the Large Magellanic Clouds in the *Gaia* data (Gaia Collaboration 2021c), the general behaviour here shows bumpy dispersions in all the populations that correlate with the oscillations in the median velocities.

Apart from the oscillations, overall we observe dispersions that are quite flat as a function of R , and even increasing at larger radii for RC stars. For the vertical velocity dispersion as a function of angular momentum (bottom panel of Fig. 11) the oscillations are even clearer. In the inner parts the dispersions decrease with L_z but this could be due to the selection effects explained above, while the profiles are overall flat in the outer

parts. We note that the geometry of our $AC20-\varpi/\sigma_\varpi > 3$ samples have larger ranges of Z for increasing R (Fig. E.2). This together with a complex selection function in the more distant regions and the approximation in the velocities of Eqs. (6) and (7) could produce artificial trends in the velocity dispersion. A similar flattening of the vertical velocity dispersion outside the solar radius was observed in Sanders & Das (2018) where the authors also discuss different biases that could explain this behaviour but also the possibility of being related to the flare (see also Mackereth et al. 2019; Sharma et al. 2020).

As for the amplitude of the dispersions, younger stars unsurprisingly present lower velocity dispersions than more evolved stars, most likely because these populations have not had the time to be heated by various internal and external processes, unlike older populations. On average, the azimuthal and vertical velocity dispersions of the EYP stars are around 8 and 5 km s^{-1} lower than those of old stars, respectively for V_ϕ^* and V_z^* .

The flattening of the velocity ellipsoid σ_z^*/σ_ϕ^* inside $R \sim 14.5$ kpc is quite homogeneous among the various populations and within the whole sample, all of them showing an azimuthal dispersion larger than the vertical component ($\sigma_z^*/\sigma_\phi^* = 0.7\text{--}0.8$, on average). The vertical random motion only exceeds the azimuthal component for RC stars beyond 15 kpc, and for EYP stars at $R = 9$ kpc and after 11 kpc. Interestingly, the random motions of the EYP stars with dispersions of values of 9 and 8 km s^{-1} for σ_ϕ^* and σ_z^* on average, respectively, are comparable to the typical velocity dispersions seen in the gas (~ 9 and 4.5 km s^{-1} respectively for neutral atomic and molecular gas for $R < 8$ kpc, Marasco et al. 2017), for a gas velocity ellipsoid assumed isotropic. Thus, in 200 Myr (the maximum age of the EYP), the youngest stars present already a slight velocity anisotropy as expected since they have oscillated of the order of one-two vertical periods.

4.2. Velocity correlations and asymmetries

We study here kinematic differences as a function of the location with respect to the Galactic mid-plane, and other phase space correlations. First, we compare the kinematics of $Z < 0$

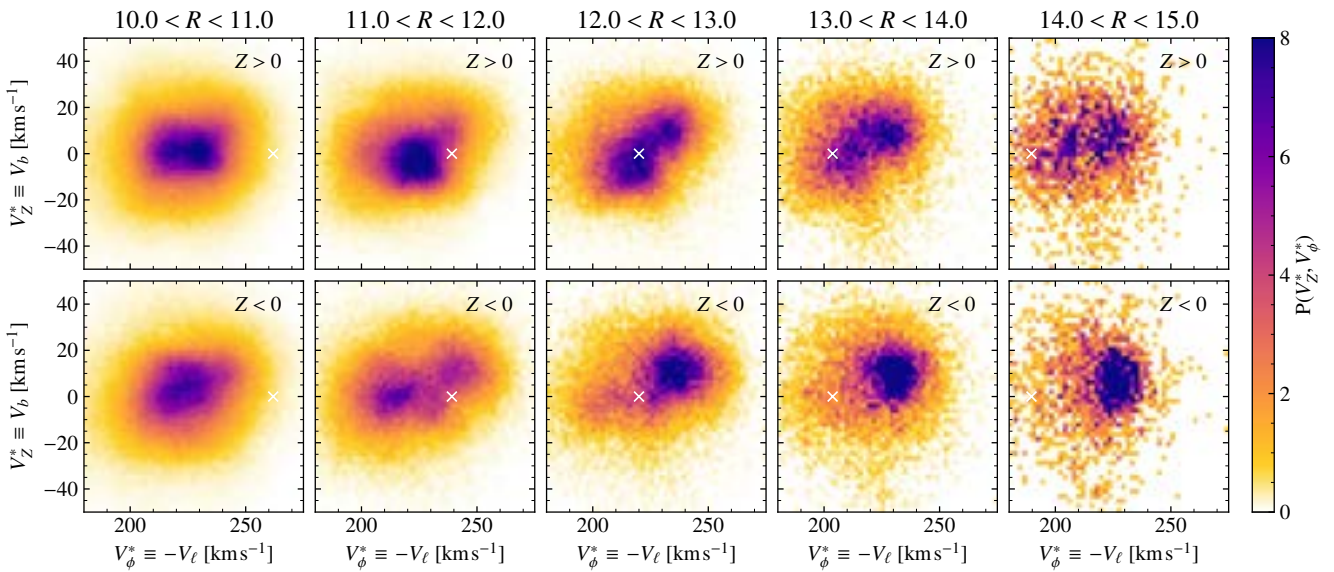


Fig. 13. Density in velocity space at different distances above and below the plane. Stellar density in the $V_\phi^* - V_Z^*$ plane, for bins in R from 10 to 15 kpc for the AC20- $\varpi/\sigma_\varpi > 3$ sample for $Z > 0$ (top) and $Z < 0$ (bottom). We see division into two components in the outer radial bins. To guide the eye a cross has been placed at V_ϕ^* corresponding to $L_z^* = 2750 \text{ km s}^{-1} \text{ kpc}$ for a point in the centre of the radial bin (see also Fig. 15).

stars with those at $Z \geq 0$ for the whole AC20- $\varpi/\sigma_\varpi > 3$ sample (Fig. 12). There is a notable asymmetry in the median velocities and the velocity dispersions (Fig. 12), starting approximately at 10–11 kpc, thus coinciding with the starting position of the large vertical velocities of Fig. 10. The rotation of $Z < 0$ stars (blue curves) clearly leads that of stars at $Z \geq 0$ (orange) beyond $R \sim 11$ kpc typically by up to 10 km s^{-1} . A significant asymmetry is also seen for $R > 10$ kpc in the vertical motion where stars at $Z < 0$ move at larger velocities than $Z \geq 0$ stars, with a difference of up to $\sim 6 \text{ km s}^{-1}$ (already noticed in Gaia Collaboration 2018c and Wang et al. 2020a for example). The asymmetries in V_Z^* start close to the Sun, though with opposite trend compared to $R > 10$ kpc. The azimuthal dispersions are comparable at lower radii but asymmetric beyond $R \sim 10.5$ kpc (larger values for $Z < 0$ stars, by up to 5 km s^{-1}) and reversing beyond 13 kpc. There is also a vertical velocity dispersion asymmetry but it is weaker ($\lesssim 1 \text{ km s}^{-1}$). In any case, the dispersions observed correspond to the typical thin disc velocity dispersions (e.g. Robin et al. 2003; Aumer & Binney 2009).

We now follow up these asymmetries by looking with more detail at the density of stars in the $V_\phi^* - V_Z^*$ plane. We show the counts in this projection in 1 kpc-wide radial bins for Galactocentric distances ranging from 10 to 15 kpc, and for the north ($Z > 0$, top) and south ($Z < 0$, bottom) Galactic plane (Fig. 13). One of the clearest features in Fig. 13 is the lack of symmetry for stars above and below the plane. Secondly, for the bins at $R > 12$ kpc we observe a bimodality where stars are sitting mainly in two clumps, one with negative V_Z^* at lower V_ϕ^* , which is more prominent in the north, and one with positive V_Z^* at higher V_ϕ^* , more conspicuous in the south. The different proportions of the clumps of the bimodality at different Z seems to be the cause of the vertical asymmetries seen at the top panels of Fig. 12, moving the median velocities to higher or lower V_ϕ^* and higher or lower V_Z^* . However, we emphasise that the bimodality appears on both sides of the disc, just in different ratios.

Figure 14 shows other phase space projections, allowing us to study this phenomenon in a more continuous way: the top panels

show V_ϕ^* as a function of R , colour-coded by either the Z position (a), the median V_Z^* (b) and the dispersion $\sigma_{V_Z^*}$ (c). At $R > 11$ kpc, the population having large V_ϕ^* ($\sim 30 \text{ km s}^{-1}$ larger than the other group) and positive V_Z^* ($\sim 10 \text{ km s}^{-1}$, blue colours in panel b) is predominantly at negative Z (red colours in panel a), and vice-versa for the population having smaller V_ϕ^* and negative V_Z^* (of about -2 to -5 km s^{-1}), as seen before. We note that the bimodal kinematic behaviour is also present at smaller R but with smaller amplitude in the vertical velocities. In fact some hints of this bimodality were seen in the maps of, for example, Khanna et al. (2019a) and Wang et al. (2020b) but those reach only 12 kpc from the Galactic centre and the bimodality appears marginally at the borders of their distributions. Additionally, we note now a clear spatial evolution, with the region at large V_ϕ^* and positive V_Z^* smoothly diminishing its V_ϕ^* when R increases. A line of constant angular momentum $L_z^* = RV_\phi^* = 2750 \text{ km s}^{-1} \text{ kpc}$ has been plotted that roughly marks the transition in the sign of V_Z^* in panel b. There is not an exact match between the transition zone in panels a and b, indicating that the dominance of one clump over the other does not occur exactly at $Z = 0$. We note that the velocity dispersion of both groups of stars is typical of the thin disc ($\sigma_{V_Z^*} \sim 15 \text{ km s}^{-1}$), as already inferred from the bottom-right plot of Fig. 12. We also see that the dispersion profiles of panels c and f are very different from the ones for the GOG mock Gaia data in Fig. E.6.

The phase spiral identified in Antoja et al. (2018) with DR2 data for stars in the immediate Solar vicinity (within $R_0 \pm 200$ pc), is illustrated in panel d of Fig. 14 now with astrometry from EDR3. The morphological change of this phase spiral (or more precisely a slice of it, centred around $Z \sim 0$ kpc, highlighted with brighter colours in panel d) is traced for radii between 8 and 10 in panel e, by plotting V_Z^* as a function of R colour-coded by V_ϕ^* . Up to $R \sim 10$ kpc, one can still see the different arms of the phase spiral at positive and negative V_Z^* (dotted lines linking panels d and e), with a diminishing envelope as one moves outwards, due to smaller restoring forces. While this has been observed already

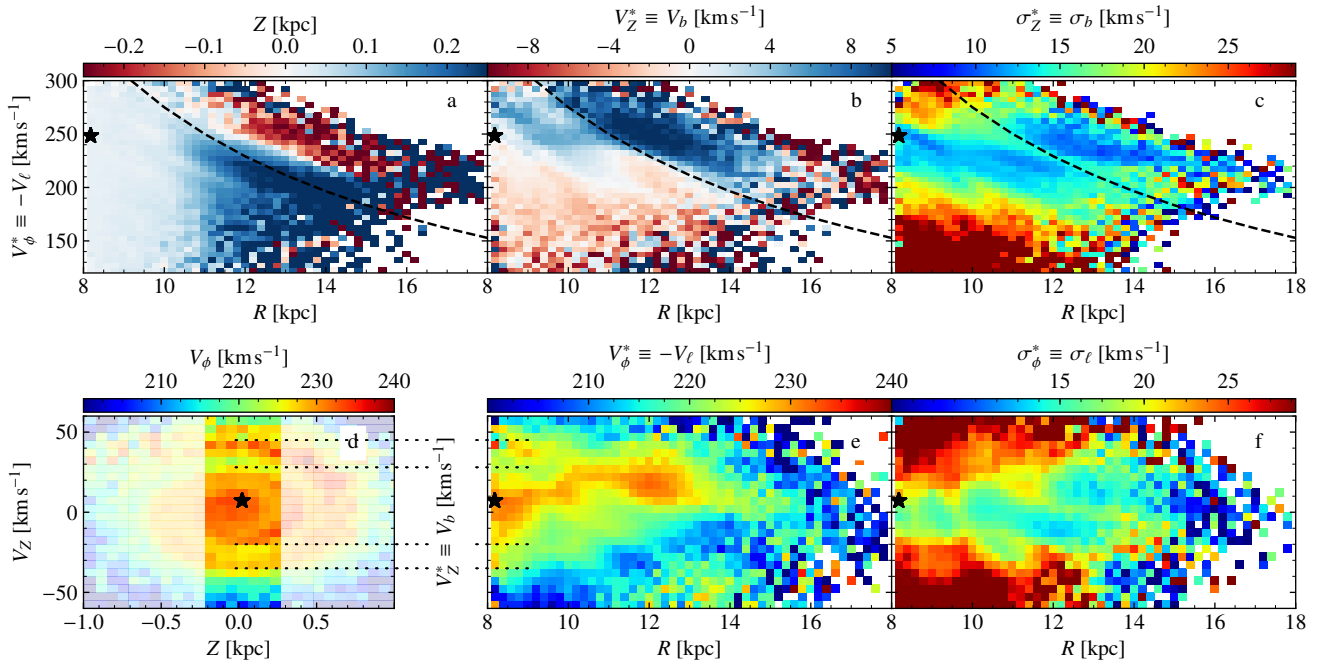


Fig. 14. Phase space projections of the Galaxy disc. The plots show for the $AC20-\varpi/\sigma_\varpi > 3$ sample: (a) median Z coordinate in the R - V_ϕ^* plane; (b) median vertical velocity V_z^* in the same projection; (c) dispersion in the V_z^* velocity in the same projection (computed as the 1.5MAD); (d) phase spiral in the 6dsample in EDR3 for stars in the Galactic radial range $|R - R_0| < 0.2$ kpc; (e) median azimuthal velocity V_ϕ^* in the R - V_z^* plane; (f) dispersion in V_ϕ^* in the same plane. The bimodality appears in the outer parts of the disc in panels *a–c*, with the separation marked with a line of constant angular momentum $L_z^* = 2750$ km s $^{-1}$ kpc. Panel *e*: evolution of a slice of the phase spiral (marked in brighter colours in panel *d*) is seen for smaller radii, while a signature related to the above bimodality is seen beyond ~ 12 kpc in panels *e* and *f*.

in Laporte et al. (2019a) for discrete ranges of R , we see it here in a continuous way. However, farther out than $R \sim 11$ kpc, we see a clump (red colours) of large V_ϕ^* and positive V_z^* dominating, which corresponds to one of the modes of the bimodality discussed above. Whether this is a manifestation of the same spiral (but blurred since we are now considering a wide range of Z given the cone geometry of the sample and because of the errors), another phase spiral at larger radius or a different phenomenon such as the warp – perhaps with the same origin – is not clear at this point.

In Appendix E we repeat some of the plots presented thus far for the GOG and UM samples (Fig. E.6). From those we conclude that selection effects due to extinction can induce some features in projections such as R - V_ϕ^* coloured as a function of Z . This is because a different extinction below and above the plane favours distinctly the different types of stars (different ages) that have different asymmetric drift (thus different V_ϕ^*) creating correlations between these variables. However, we do not observe any special vertical kinematics for these features in the mock data. We also checked that the effects of the zero point in parallax does not induce or remove the features observed but merely change the distance scale with the pattern arriving farther or closer, independently whether a constant ZP or ZP₅₆ is used (Fig. D.2). Moreover, these features preferentially occupy positive or negative Galactic latitudes but do not correlate with the smaller scale checked patterns seen in the astrometry. We note also that the stars participating in this phenomenon are relatively bright stars (Fig. E.7), thus with good astrometry in general. Also the difference of 10 km s $^{-1}$ seen in the velocities of the two distinct features mentioned above which are at a typical distance of 4 kpc, correspond to a proper motion difference

of around 0.5 mas yr $^{-1}$, which is much bigger than any known systematics.

Finally, Fig. 15 shows the angular momentum-vertical velocity (L_z^* , V_z^*) space, coloured by density in V_z^* at each L_z^* (top) and average Z coordinate (bottom). In this plot, we see oscillations in V_z^* for the smaller L_z^* (better seen in the top panel of Fig. 11, and seen also in Huang et al. 2018 and Cheng et al. 2020) that likely correspond to the vertical oscillations also seen in the top right panel of Fig. 10 at nearby Galactocentric radii. Most notably, these plots show that the clumpy features seen for $R > 11.5$ kpc in Fig. 13 correspond to a clear break in the (L_z^* , V_z^*) density at ~ 2750 km s $^{-1}$ kpc rather than a smooth transition. We note that when we separate our sample into young population (YP+EYP), main sequence (IP+OP) or Giants (Fig. E.8), this trend is seen for all the populations (albeit most clearly in the young one, as it has the lowest velocity dispersion) implying that this break is most likely of dynamical origin. In particular, the change in proportions between the two populations that we see in Fig. 13 as we move outwards is related to the fact that the population with $L_z^* \lesssim 2750$ km s $^{-1}$ kpc (and $V_z^* < 0$) does not reach as large radii as the population with $L_z^* \gtrsim 2750$ km s $^{-1}$ kpc (and $V_z^* > 0$ km s $^{-1}$). According to the bottom panel of Fig. 15, and as seen above, the part of the disc at lower angular momentum L_z^* corresponds to stars predominantly at positive Z while the one with higher L_z^* mostly has negative Z , though without perfect one-to-one correlation.

4.3. Small scale velocity structures

Apart from the two clumps discussed in Sect. 4.2, finer substructures in the phase space of the disc can already be seen in the

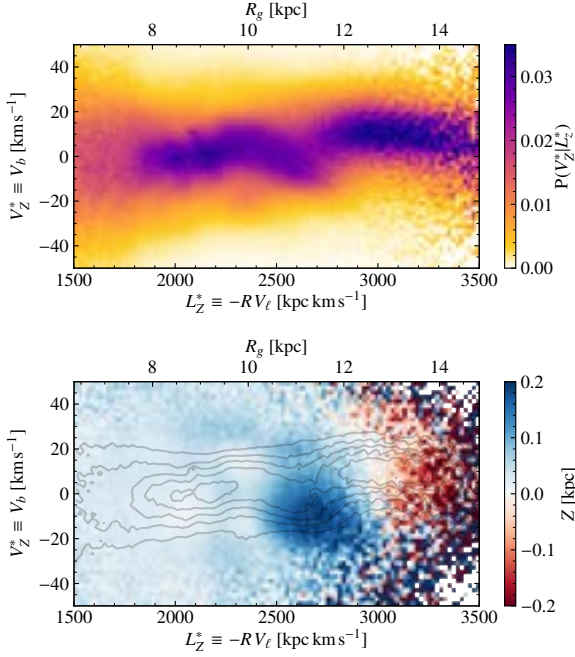


Fig. 15. Structures in vertical velocity and angular momentum. *Top*: column normalised histogram of star numbers in the $L_z^* - V_z^*$ plane for the AC20- $\varpi/\sigma_\varpi > 3$ sample (the colour represents the fraction of stars in a given L_z^* bin that have a certain V_z^*). *Bottom*: average Z of stars in each bin in $L_z^* - V_z^*$ in our AC20- $\varpi/\sigma_\varpi > 3$ sample. Contours are the same as the colour plot in the *top panel*. To guide the eye, we also show an approximate guiding radius $R_g = L_z^*/(236 \text{ km s}^{-1})$.

top panels of Fig. 14 for nearby radii. These structures are better visualised in Fig. 16 showing the 2-dimensional histogram of the $V_\phi^* - R$ projection (panel a). Diagonal ridges (i.e. substructures with decreasing V_ϕ^* as a function of R) can be seen, as already discovered in the *Gaia* DR2 (Antoja et al. 2018; Kawata et al. 2018). To enhance the contrast of these substructures, in panel b we show the density relative to a smoothed density obtained from a Gaussian filter $\frac{N - N_s}{N_s}$, where N are the counts and N_s are the smoothed counts with a $\sigma = 5$ times the bin size (similar to what is done in Laporte et al. 2019a). Panels c–e show this relative density for different stellar types. We do not note any difference between using $ZP = -17 \mu\text{as}$ and Z_{56} except for the already mentioned distance scaling.

The location of the main ridges obtained in Ramos et al. (2018) with the DR2 *Gaia* RVS sample are over-plotted with colour lines in Figs. 16b–e. Following their notation, we can identify the ridges associated to Hercules, Hyades, L18 (with a different slope compared to the rest) and one that could be linked to L16 or the so called hat (e.g. Gaia Collaboration 2018c, $V \sim 40 \text{ km s}^{-1}$ on their Fig. 22) – also related to L14 and L17.

Interestingly, for the YP the Sirius ridge appears to have slightly higher V_ϕ^* velocities than the marked ridge (red line), as if following the asymmetric drift relations, and the ridges look thinner than in the RG or RC plots. We estimate the fraction of stars forming the ridges by calculating $\frac{\sum(N - N_s)_{>0}}{\sum N_s}$. These fractions are 30, 13, 8, 8% for the EY, YP, IP and OP, respectively. The fractions are 11, 14 and 8% for the RG, RC and all AC20- $\varpi/\sigma_\varpi > 3$ stars, respectively. This fraction depends on the σ used to smooth the distribution but the relative trends are the same, from which we see that the younger the population,

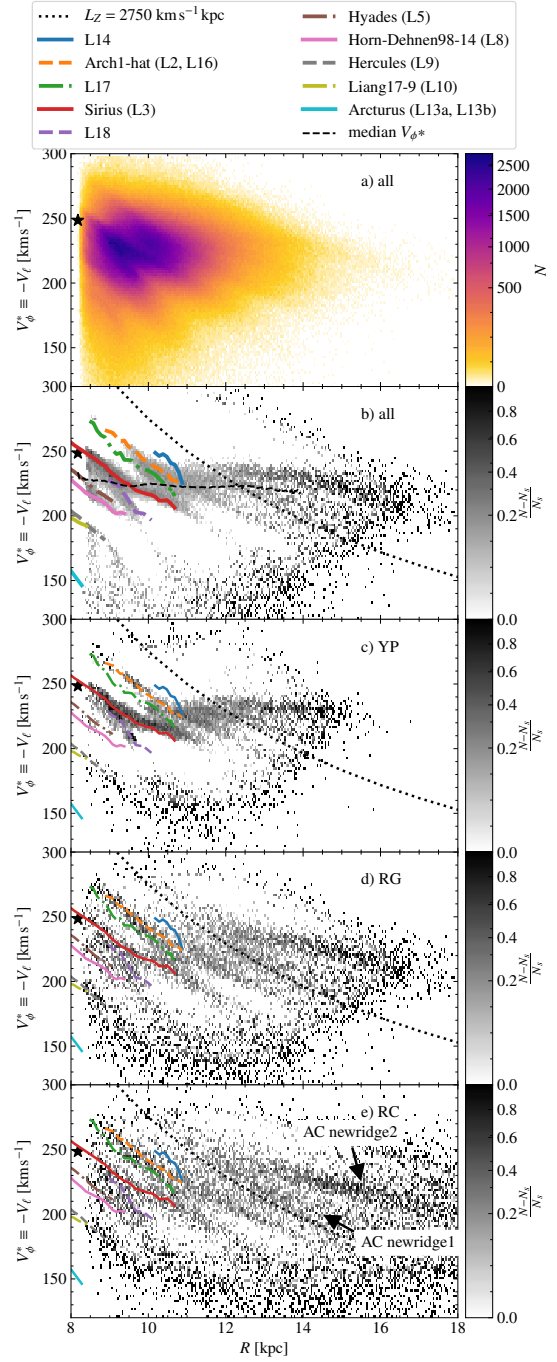


Fig. 16. Substructures in the $R - V_\phi^*$ projection in the anticentre direction. (a) Number counts in the $R - V_\phi^*$ plane in bins of size $\Delta R = 0.02 \text{ kpc}$ and $\Delta V_\phi^* = 1 \text{ km s}^{-1}$ for all stars in the AC20- $\varpi/\sigma_\varpi > 3$ sample. (b) Same but applying a substructure mask to highlight the ridges (see text). (c–e) Same as b but for different stellar types. We also plot: some ridges from Ramos et al. (2018) with coloured lines, the separation of the bimodality (black dotted line), and the median velocity (black dashed line in panel b). We see the ridges extending beyond their limits in DR2 and new ridges resolved here for the first time.

the higher the fraction of stars in substructures. On the other hand, we do not have enough stars in the lower V_ϕ^* region in any of the populations to notice the low angular momentum ridges suggested in Laporte et al. (2020b).

More importantly, in Fig. 16 the ridges are now seen at much larger distances than before. The Sirius ridge is detected up to $R \sim 12.5$ kpc, while in *Gaia* DR2 a sophisticated method to detect very low contrasts was needed to reach even $R \sim 11$ kpc (Ramos et al. 2018). We can also spot three ridges that reach outer regions of the disc, up to 16 kpc and beyond in the case of the RC. The one at lowest V_ϕ^* could be the extension of L16. The other two were previously unknown and have been marked with arrows in the bottom panel (new anticentre ridges 1 and 2). The new structures do not point towards $V_\phi^* \sim v_{c,\odot} + V_\odot$ and $R = R_0$ (black star in the panels) as expected for structures stretched by errors in distance (see Fig. 9). In addition, we do not see any similar ridge induced by selection effects, uncertainties, or extinction, in the GOG equivalent sample.

In the panels b–e of Fig. 16 we also plot the line of angular momentum $L_z^* = 2750 \text{ km s}^{-1} \text{ kpc}$ (dotted black line) which marks the approximate separation of the bimodality described in Sect. 4.2. While this line seems to coincide with the new anticentre ridge 1 (especially in panel e), no dynamical connection is clear at this stage. The median rotation velocities from Fig. 10 are over-plotted as a black dashed line in panel b and we see that the bump at around 10 kpc seems linked to the appearance of the L16 ridge that, with higher V_ϕ^* , moves the median curve slightly upwards. The connection between ridges and bumps in the rotation curve was already suggested by Martinez-Medina et al. (2019, 2020). The bump at 13 kpc could also be connected to the new anticentre ridge 2.

In Fig. 14a, we see some correspondence between the median Z and the density ridges seen in Fig. 16 (e.g. the white ridge in panel a with lower median Z overlaps with the Sirius ridge). Similarly, in Fig. 14b the ridges exhibit a complex pattern of positive and negative vertical velocities, thus indicating coupling between in-plane and off-plane kinematics. These effects were also noticed in *Gaia* DR2 with the RVS sample (Khanna et al. 2019b; Laporte et al. 2019a), where the ridges were stronger at lower Z and had some amplitude in V_z^* though typically lower than 5 km s^{-1} .

5. Halo, thick disc, and distant structures

In this section, we investigate several constituents of the Galaxy through the powerful combination of *Gaia* astrometry and photometry. In Sect. 5.1 we look at the stars of high tangential velocity which are contributed by the halo and the hot thick disc and secondly, in Sect. 5.2 we explore the structures in the outer parts of the Galaxy disc.

5.1. Halo and thick disc

Our goal in this section is to establish the extent and properties of the stellar halo populations beyond the solar vicinity and towards the galactic anticentre. To enhance the contribution of halo stars and partially mitigate the effects of high-extinction near the disc plane, we used the ACV sample, defined in Sect. 2.2, with an additional selection of $|b| < 40^\circ$. We selected on $\varpi/\sigma_\varpi > 5$ and compute distances as the inverse parallax. Since we are interested in precise intrinsic colours and magnitudes, we chose only stars that have G -band extinction $A_G < 1.0$. Here the extinction is computed using the Schlegel et al. (1998) maps (with the correction of Schlafly & Finkbeiner 2011) and a Cardelli et al. (1989) extinction curve with $R_V = 3.1$. Although this extinction correction does not yield intrinsic magnitudes as accurate as in Appendix B, the main goal here is simply to remove

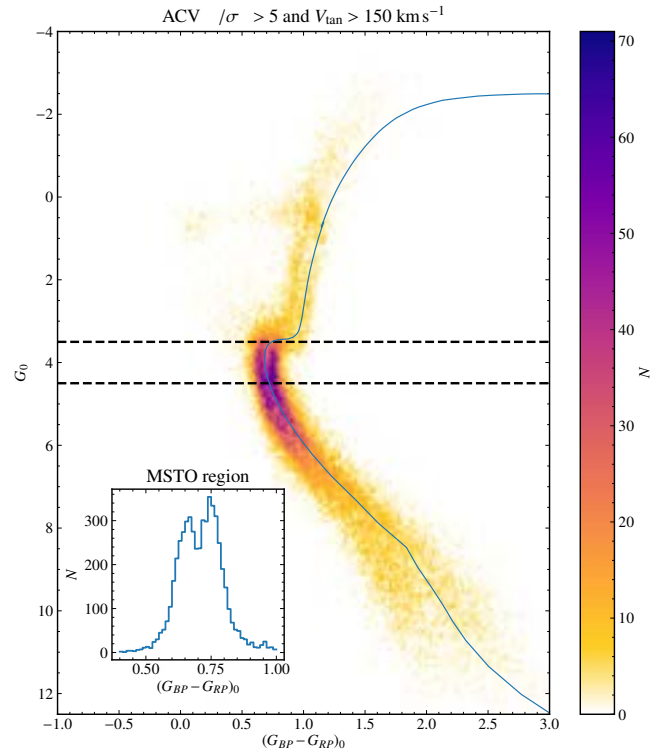


Fig. 17. Red and blue sequences for high tangential velocity stars. $G_{RP} - G_{BP}$ vs. G Hess diagram for the ACV sample with $|b| < 40^\circ$ and with a $\varpi/\sigma_\varpi > 5$ and $V_t > 150 \text{ km s}^{-1}$. A PARSEC isochrone with $[M/H] = -0.5$ and age of 11 Gyr is shown in blue (but shifted by 0.04 in colour and 0.2 in magnitude in order to match the gap between blue and red sequences). The inset histogram shows the colour distribution in the magnitude range of the MSTO (shown as dashed lines in the main figure). A clear separation in two sequences is clearly seen as originally noted in Gaia Collaboration (2018a) with DR2 data. An animated version of this figure for varying V_t limits is available online.

high-extinction regions from our analysis, while producing accurate enough colours at large distances.

Following the approach of Gaia Collaboration (2018a), we focus on the HR diagram for stars in the ACV sample that pass the cuts described above. We find that when selecting only stars with high heliocentric tangential velocity V_t (Eq. (8)), two sequences arise as shown in Fig. 17, and that at the value of $\sim 150 \text{ km s}^{-1}$ both sequences seem to be found in equal numbers around the main-sequence turn-off point. For completeness, see also our animation of how the HR diagram varies as V_t is increased in 5 km s^{-1} slices that is available online (see caption). When V_t is low, there is a significant contribution from the thin and the canonical thick discs, whereas at $V_t \gtrsim 250 \text{ km s}^{-1}$ mainly the blue sequence (that locally is dominated by stars from the accreted *Gaia*-Enceladus-Sausage) is apparent.

In Fig. 17 the double sequence extends beyond the turn-off point, but with fewer luminous stars in the red sequence than in the blue one, suggesting that the distance distribution of the two populations is different (since at the largest distances only the brightest stars are apparent, and there are fewer of these on the red sequence). In order to select stars in either sequence we use a PARSEC isochrone (Bressan et al. 2012; Marigo et al. 2017) with $[M/H] = -0.5$ and age of 11 Gyr (blue line). The isochrone was shifted by 0.04 in colour and 0.2 in magnitude in order to match

the gap between blue and red sequences. Both the isochrone and extinction coefficients use *Gaia* DR2 transmission curves.

We now explore the dynamical distributions of the stars belonging to these two sequences in more detail. To this end we explore the velocity distribution in V_ℓ and V_b (Fig. 18), for three cylindrical galactocentric distance bins for the stars in the blue (left) and red (right) sequences. We note that at the higher latitudes within this sample V_Z^* becomes a poorer approximation to V_ℓ , but that is still a reasonable approximation to the non-radial, non- V_ϕ velocity of stars, and to low latitude stars. On the other hand, V_ℓ is good proxy for V_ϕ given the small range in ℓ . The densest structure at $V_\phi^* \sim 220 \text{ km s}^{-1}$ is comprised mainly of disc stars, while the more extended and sparser structures belong to the halo and thick disc. Firstly, we note the presence of the [Helmi et al. \(1999\)](#) streams in the top-left panel at $(-V_\ell, V_b) \sim (150, -250) \text{ km s}^{-1}$ (indicating that these streams are a relatively local feature, in agreement with the results and predictions of [Koppelman et al. 2019](#)). We see, however, some hints of structures at similar velocities (and mirrored ones) in the second left panel of more distant stars that could potentially be related to these known streams. For the local sample (top panels) we observe a higher V_b velocity spread for the halo (i.e. at $V_\ell \sim 0$) blue sequence stars compared to the red sequence. In the intermediate distance bin (middle panels) the velocity distribution of red sequence stars barely extends to $V_\ell \sim 0$ and for the most distant stars (bottom panels) only the blue sequence is apparent in the halo population, with the red sequence mostly appearing as a low-dispersion disc-like component.

Similar conclusions can be drawn from Fig. 19 which shows the distribution of V_b velocities for the blue and red sequence for the same distance bins (columns) as in the previous figure, and for five V_t selections (rows). We note again that the red-sequence distribution generally has a lower velocity dispersion than the blue sequence stars (indicated with numbers for cases with at least 50 stars). We also see that for $V_t \geq 100 \text{ km s}^{-1}$ the dispersion increases significantly, indicating the transition from the canonical thick disc to a hotter component. For the more distant bins, the contribution of this hot thick disc becomes smaller (bottom right panels), and it is basically absent beyond 14–17 kpc (whereas the canonical thick disc still is apparent in the top panels at these radii). On the other hand, the blue sequence is apparent at all radii, and has a relatively large V_b velocity dispersion.

Therefore, the analyses presented in this section show that the hot thick-disc component, which locally has been associated with the heated disc at the time of the merger with *Gaia*-Enceladus-Sausage, has a smaller extent presently than the canonical thick disc. This suggests that the disc present at that time was smaller in size, as indeed expected from cosmological models. A more quantitative estimate of its size would require a careful assessment of the density distribution of the older stars in the red sequence, which is beyond the scope of this work. On the other hand, we see that the component locally associated with *Gaia*-Enceladus-Sausage extends out to large distances from the Sun, as we detect the presence of a retrograde component out to $\sim 17 \text{ kpc}$ from the Galactic centre.

5.2. Distant structures

Studying the outskirts of the disc is a difficult task since the anti-centre is mostly outshone by the nearby stars which are more numerous due to both the density gradient of the Galaxy and the magnitude limitations inherent to any survey. The majority of the studies of the outer disc detected unexpected overdensities in

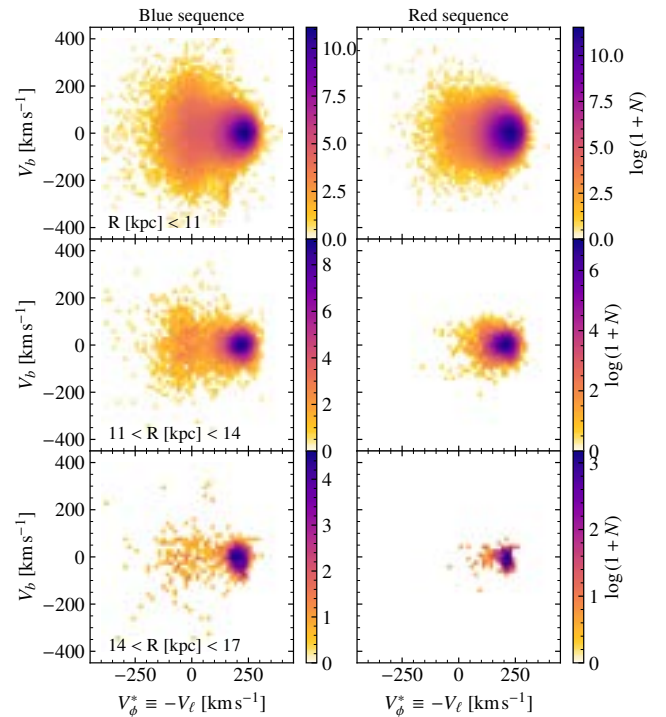


Fig. 18. Velocity distribution of the blue and red sequences. $-V_\ell \sim V_\phi^*$ vs. V_b distribution showing in the *left (right) column* the stars in the blue (red) sequence. Each row shows the distributions for a given distance slice, indicated in the left panels. The stars with low rotation (even the retrogrades ones) are far more prominent in the blue sequence and extend to larger Galactocentric radii.

counts such as Monoceros and ACS and focused on a specific stellar type, generally main sequence turn-off stars or M giants. An alternative way is now possible with *Gaia*, which allows us to detect them by applying the right astrometric selection. First, we can significantly reduce the amount of foreground contamination with a cut in parallax selecting only stars with $\varpi < 0.1 \text{ mas}$. By doing so, we guarantee that most of the stars closer than 10 kpc are not selected, although the probability of failure is related to the parallax error of the source (the fainter sources being more likely to pass the filter regardless of their true distance). Then, we applied a kinematic selection since the proper motion signatures of these structures, given that they are relatively far from the Sun, are significantly different from the nearby disc and halo stars. The latter tend to have large proper motions due to the large relative velocity with respect to the Local Standard of Rest, while the former also tend to have large proper motions, but in this case due to the small heliocentric distance. Figure 20 is an example of such parallax and kinematic selection ($-1 < \mu_\alpha^* < 1 \text{ mas yr}^{-1}$ and $-2 < \mu_\delta < 0 \text{ mas yr}^{-1}$) where, in contrast to Fig. 1, we can observe a perfectly defined and thin ACS, as indicated by the arrow. The difference between DR2 (left) and EDR3 (right) is clear: we now have more stars (7 624 697 compared to 5 951 302), mostly due to the higher completeness of stars with proper motions in EDR3, and the sample is less affected by the scanning law and other artefacts.

In the first column of Fig. 21 we show the proper motion 2d histograms for different slices in latitude around the anticentre ($170^\circ < \ell < 190^\circ$) using the sample ACV, now with the astrometric and photometric filters, as well as the parallax zero-point correction. As we move from the north to the south Galactic

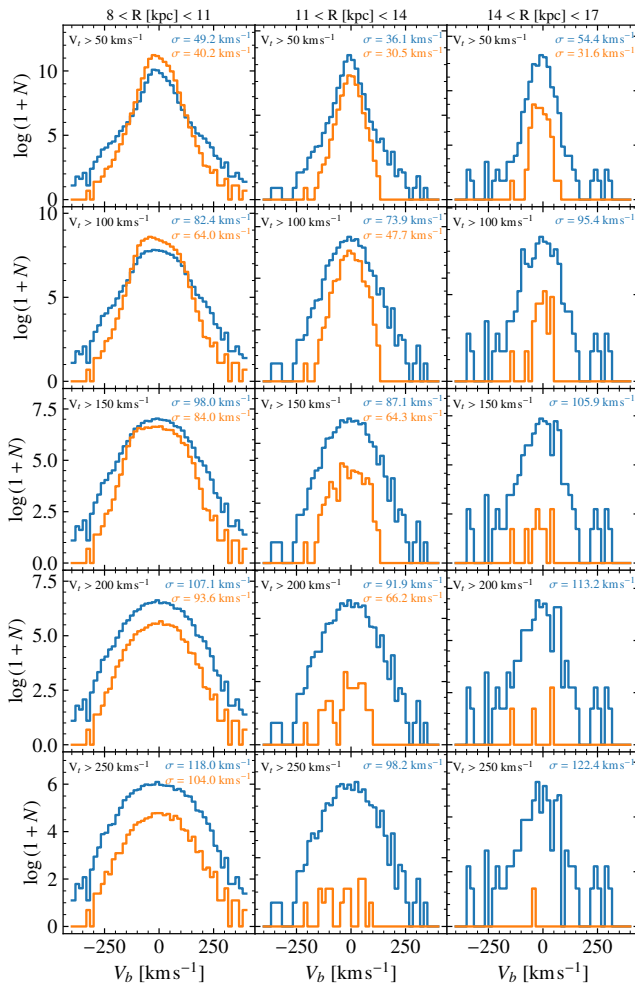


Fig. 19. Vertical tangential velocities V_b for the blue and red sequences. The plots are for different distance slices, indicated in the top of each column. Each row shows a different V_t selection, indicated in each panel. The blue (orange) curve shows the distribution for the blue (red) sequence. The different relative contribution of the sequences in the different panels is indicative of the spatial distribution of the accreted component and the ancient heated disc, and in particular of a shorter extent of the later one.

hemisphere (top to bottom), different structures can be observed. We examine them by selecting stars in the rectangles A to H and plotting their Colour-Magnitude diagrams (CMDs) in the second and third columns using $G - G_{RP}$ instead of $G_{BP} - G_{RP}$ since, as exposed in [Riello et al. \(2021\)](#) – see their Fig. 26 –, the flux in the BP band can be overestimated for faint sources.

First, we note that the large concentration of sources close to the proper motion origin in the boxes A and G are mostly quasars for several reasons. Firstly, they are faint and too blue, with $G - G_{RP} < 0.5$ mag, which is equivalent, incidentally, to the cut used in [Newberg et al. \(2002\)](#) ($g - r < 0.3$ mag) to remove the SDSS quasars⁸. Secondly, the fraction of primary sources (`astrometric_primary_flag`), a significant fraction of which are quasars ([Lindgren et al. 2018](#)), is abnormally high in both A and G. Finally, $\sim 32\%$ of the sources in A and $\sim 75\%$ in G are found in the `agn_cross_id` table.

⁸ We used the values in Table 5 from [Jordi et al. \(2010\)](#) to convert the SDSS colours to *Gaia* colours.

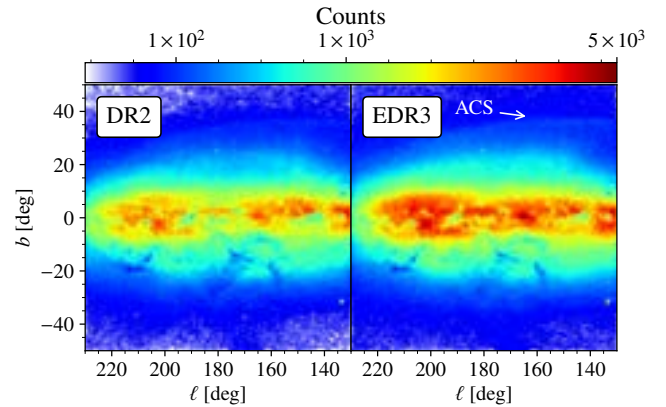


Fig. 20. Counts in the sky for a selection of stars that favours the outer disc structures. The selection is for stars with $\varpi < 0.1$ mas, $-1 < \mu_{\alpha^*} < 1$ mas yr⁻¹ and $-2 < \mu_{\delta} < 0$ mas yr⁻¹. *Left:* DR2 (we observe marks of the scanning law). *Right:* EDR3 (with more stars and better homogeneity) without filters nor parallax zero-point correction. The ACS can be seen more clearly in the right panel.

More interestingly, box A contains other kinematic structures apart from the aforementioned quasars. There is a more extended giant branch formed by the ACS (cf. Fig. 2 from [Laporte et al. 2020a](#)) and, tentatively, two fainter tips of a giant branch that could be related to the Sagittarius stream (similarly to box C, as explained below). The other box (B) at the same latitude corresponds to the distribution of halo stars, their proper motions larger due to the Sun’s reflex motion and their CMD compatible with an old isochrone at ~ 10 kpc or farther, where stars accumulate due to our parallax cut. In the second row, panel C contains parts of both Monoceros, which provides the giant branch, a well defined RC and a very blue turn-off consistent with previous observations (e.g. [Newberg et al. 2002](#); [Yanny et al. 2003](#)), and the leading tidal tail of Sagittarius, which is only evident by its AGBs at magnitudes between 17 and 18. Boxes D and F are dominated by the disc which, after the selection in parallax, is expected to have a thick main sequence created by faint dwarfs with large parallax uncertainties, and a few Red Giants⁹ above magnitude $G \sim 17$ mag.

In the south, at latitudes $-30 \text{ deg} < b < -20 \text{ deg}$, we observe that the CMD of the small proper motion population is dominated by two RCs (panel E), the densest at magnitude ~ 17 mag and the other at ~ 15.5 mag. To confirm their existence, we have obtained the Gaussian kernel of $G^* = G - 1.95(G_{BP} - G_{RP})$, therefore marginalising the apparent magnitudes along the extinction line (see Sect. 2.4). This kernel (shown within panel E) presents two overdensities corresponding to each of the mentioned RCs. By approximately selecting stars in these clumps and computing their distances assuming an absolute magnitude of the RC of $M_G = 0.495$ ([Ruiz-Dern et al. 2018](#)) and the extinction by [Schlegel et al. \(1998\)](#) – and thus, upper limits –, we find that they are located at an average heliocentric distance of 9 and 14 kpc with variance of 3 and 2 kpc, for the bright and faint clumps, respectively. These corresponds to Galactocentric cylindrical radii of around 16 and 21 kpc, and heights below the plane of -4 and -6 kpc, respectively. With this it is very likely that the bright RC corresponds to a nearby south extension of Monoceros

⁹ A RC star fainter than $G \sim 15$ mag at latitudes $b > 10^\circ$ is bound to be higher than 2 kpc from the disc, which is unlikely, but stars brighter than that tend to have a reliable parallax and are therefore more likely to be removed with our parallax cut.